Check for updates

JGR Planets

RESEARCH ARTICLE
10.1029/2026JE009866

New Constraints on the Lunar Crust and Upper Mantle From Multiple Geophysical Data Sets

Xiang Zhang[1,2], Philippe Lognonné[1], Henri Samuel[1], Taichi Kawamura[1], Mélanie Drilleau[1], Mark Wieczorek[1], Zongbo Xu[1,3], and Keisuke Onodera[4]

[1]Université Paris Cité, Institut de physique du globe de Paris, CNRS, Paris, France, [2]Now at Key Laboratory of Deep Petroleum Intelligent Exploration and Development, Institute of Geology and Geophysics, Chinese Academy of Sciences, Beijing, China, [3]Now at Norwegian Geotechnical Institute, Oslo, Norway, [4]Institute for Planetary Materials, Okayama University, Tottori, Japan

Key Points:

- We performed an integrated geophysical inversion to investigate the structure of the lunar crust and upper mantle
- A refined crustal model provides an updated global Moho depth of approximately 35 km and indicates a lower uppermost mantle velocity
- The new model provides improved constraints on the porosity, density, bulk Th and Al abundances of the lunar crust

Supporting Information:

Supporting Information may be found in the online version of this article.

Correspondence to:

X. Zhang,
zxiang@ipgp.fr

Citation:

Zhang, X., Lognonné, P., Samuel, H., Kawamura, T., Drilleau, M., Wieczorek, M., et al. (2026). New constraints on the lunar crust and upper mantle from multiple geophysical data sets. *Journal of Geophysical Research: Planets*, *131*, e2026JE009866. https://doi.org/10.1029/2026JE009866

Received 19 APR 2026
Accepted 22 OCT 2026

Author Contributions:

Conceptualization: Philippe Lognonné
Methodology: Xiang Zhang, Henri Samuel, Taichi Kawamura, Mélanie Drilleau, Mark Wieczorek, Zongbo Xu, Keisuke Onodera
Project administration: Philippe Lognonné
Software: Xiang Zhang, Henri Samuel, Mélanie Drilleau
Supervision: Philippe Lognonné, Henri Samuel, Taichi Kawamura
Validation: Taichi Kawamura
Writing – original draft: Xiang Zhang

© 2026 The Author(s). Journal of Geophysical Research: Planets published by Wiley Periodicals LLC on behalf of American Geophysical Union.
This is an open access article under the terms of the Creative Commons Attribution License, which permits use, distribution and reproduction in any medium, provided the original work is properly cited.

Abstract Determining the crust–mantle boundary of the Moon has been an important topic in lunar interior studies. However, strong seismic scattering in the lunar subsurface has made it challenging to identify clear crustal reflections or converted seismic phases. In addition, the limited epicentral distances of recorded moonquakes restrict direct constraints on the lunar crust from first-arriving seismic waves. Consequently, the Moon's crustal structure remains poorly constrained due to the limited availability of seismological evidence. Through joint analysis of seismic, topographic, and gravity data, while accounting for seismic velocity variations predicted by thermal modeling, we obtain new ray tracing results and present new insights on the lunar crust and upper mantle structure. Our results constrain the average global Moho depth to 35.1 ± 2.6 km. Additionally, our results indicate slightly lower seismic velocities in the uppermost mantle than previously estimated, at approximately 7.5 km/s. Introducing the thermal model into the inversion further allows us to constrain the Moon's surface heat flow, with an average value of 10.7 ± 0.8 mW/m^2, which is consistent with the heat flow measurements obtained during the Apollo mission. The refined crustal thickness provides a structural basis for estimating the Moon's bulk Al and Th abundances. The model also better constrains the porosity, density, and radiogenic heat production of the lunar crust, and provide new implications for a pyroxene-rich upper mantle composition.

Plain Language Summary Understanding where the Moon's crust transitions into the mantle has long been an important goal in studying the Moon's interior. However, the limited number of usable seismic signals, together with complex and long-lasting seismic coda waves, have made this boundary difficult to identify. In this study, we combined seismic, gravity, topographic, and thermal data within a 3D modeling framework to better constrain the Moon's internal structure. Our results show that the crust–mantle boundary lies at an average depth of 35.1 ± 2.6 km, significantly reducing the uncertainty associated with this problem. The uppermost mantle exhibits slightly lower seismic velocities than previously estimated, at approximately 7.5 km/s. By including a thermal model in our analysis, we can also estimate how much heat is released from the Moon's surface. Our results indicate an average surface heat flow of 10.7 ± 0.8 mW/m^2, consistent with measurements from the Apollo mission. The updated lunar crustal thickness helps reduce the uncertainties in the estimated bulk Al and Th abundances of the Moon. These results also place new constraints on the porosity, density, and heat production of the lunar crust, and provide new implications for a pyroxene-rich upper mantle composition.

1. Introduction

Our current understanding of the Moon, including the giant impact hypothesis and the lunar magma ocean hypothesis, has been developed based on an integrated set of constraints on its interior structure, composition, and thermal state derived from multiple geophysical and geological observations (Jolliff et al., 2006). Among these, the lunar interior structure, constrained primarily by geophysical and geodetic observations, provides critical evidence supporting these hypotheses. However, owing to the limited availability of lunar data, existing constraints still involve considerable uncertainties and limitations, leaving many details of these hypotheses unresolved (Andrews-Hanna et al., 2023). In particular, the global average crustal thickness is a key parameter in lunar models and has important implications for determining the abundance of chemical elements, crustal porosity, density, and surface heat flow. Although previous studies have provided important insights (Chenet et al., 2006;

Writing – review & editing: Xiang Zhang, Philippe Lognonné, Henri Samuel, Taichi Kawamura, Mélanie Drilleau, Mark Wieczorek, Zongbo Xu, Keisuke Onodera

Goins et al., 1981; Khan & Mosegaard, 2002; Kim et al., 2025; Lognonné et al., 2003; Nakamura, 1983; Toksőz et al., 1972; Vinnik et al., 2001), significant uncertainties in the lunar crustal structure remain.

Toksőz et al. (1972) constrained the compressional-wave velocity structure down to depths of approximately 100 km by analyzing *P*-wave arrivals generated by the Saturn IV B (SIVB) and lunar module (LM) impacts, identifying a crust-mantle boundary at about 65 km depth. Goins et al. (1981) proposed that the lunar crust is essentially two-layered, with a sharp crust-mantle interface at a depth of 55–60 km. Khan and Mosegaard (2002) inferred a shallower crust-mantle interface, revising the crustal thickness to approximately 38 km. These earlier studies primarily relied on first-arriving *P* waves from artificial impacts near the Apollo stations to constrain lunar crustal structure; therefore, the results mainly reflect local characteristics around the Apollo seismic network. However, due to the limited number of seismic events available for crustal inversion, almost no first-arrival seismic rays remained confined within the crust, preventing direct constraints on crustal velocities; consequently, these studies inevitably faced an inherent trade-off between crustal seismic velocities and layer thicknesses.

Several efforts have also used secondary seismic phases to constrain the lunar crust-mantle interface. Vinnik et al. (2001) used *S*-receiver function analysis to detect an Sp phase converted beneath the Apollo Station 12, which was interpreted as originating from the crust-mantle boundary. Lognonné et al. (2003) used the results of this receiver function analysis to infer a 30 km-thick lunar crust and a boundary between the upper and lower crust at a depth of 12 km beneath the Apollo Station 12. Kim et al. (2025) applied polarization analysis to isolate phases arising from the lunar crust-mantle boundary, yielding new estimates of the global average crustal thickness, ranging from 29 to 47 km. Furthermore, auto-correlation methods have also been used to indicate the presence of crust-mantle discontinuities (Torrent Duch et al., 2025). Notably, strong seismic scattering in the lunar megaregolith complicates the identification of clear crustal reflections or converted seismic phases (Shi et al., 2023), making the selection of secondary phases particularly challenging. The number of usable secondary phases is limited and subject to considerable uncertainty (Khan et al., 2013), so constraints on the multilayered structure of the lunar crust derived from these phases remain highly uncertain.

While the upper mantle is reasonably sampled by seismic rays, substantial uncertainties in the available data (seismic arrival time data set) lead to considerable variability, with previously inferred *P*-wave velocities ranging from 7.57 to 8.90 km/s (Gagnepain-Beyneix et al., 2006; Khan et al., 2000; Lognonné et al., 2003; Nakamura, 1983; Toksöz et al., 1974). Consequently, the inversion suffers from a trade-off between crustal velocities and thickness and between crustal and mantle properties, leading to substantial uncertainties in the inferred structure (Khan & Mosegaard, 2002; Nakamura, 1983). In addition, uncertainties in the seismic velocities of the upper mantle limit our ability to reliably constrain its composition, physical structure, and thermal state (Khan et al., 2006).

Gravity field observations provide an additional approach to constraining the structure of the lunar crust, particularly its lateral variations. Chenet et al. (2006) presented the first comparison between Apollo seismic estimates of crustal thickness and the Clementine/Lunar Prospector gravity and topography models. They inverted however only the crustal thickness from *P* and *S* arrival times and found a global average crust thickness of 40 ± 5 km and a thickness of 32 ± 7 km below Apollo 12/14 landing sites. The higher-quality data obtained from the Gravity Recovery and Interior Laboratory (GRAIL) mission help better constrain global lateral variations in lunar crustal thickness and crustal porosity. Wieczorek et al. (2013) assumed an anchor point of 30 km (Lognonné et al., 2003) or 38 km (Khan & Mosegaard, 2002) at the Apollo 12/14 landing sites to estimate the global average crustal thickness at 34 km or 43 km, respectively. However, this range (34–43 km) likely underestimates the true uncertainty in the average thickness, as it does not account for errors in the anchoring point or local uncertainties in the gravity model (Zhang et al., 2026). If these errors are taken into account, the uncertainty range should be much larger (Kim et al., 2025).

With the exception of Chenet et al. (2006), previous seismic studies generally did not take into account the topography of the lunar surface and crust-mantle discontinuity, despite it being evident from gravity data. This simplification creates systematic errors in seismic ray tracing. Furthermore, lateral variations in crustal thickness are producing mantle temperature variations (Schumacher & Breuer, 2006; Ziethe et al., 2009) and consequently seismic velocity variations (Sobolev & Babeyko, 1994). In other words, thick crust might generate positive mantle temperature variations and therefore be associated with lower seismic velocities relative to regions with thin crust. Therefore, in this study, we constructed a global 3D model of the Moon that integrates surface

21699100, 2026, 11, Downloaded from https://agupubs.onlinelibrary.wiley.com/doi/10.1029/2026JE009866 by Okayama University, Wiley Online Library on [11/11/2026]. See the Terms and Conditions (https://onlinelibrary.wiley.com/terms-and-conditions) on Wiley Online Library for rules of use; OA articles are governed by the applicable Creative Commons License

21699100, 2026, 11, Downloaded from https://agupubs.onlinelibrary.wiley.com/doi/10.1029/2026JE009866 by Okayama University, Wiley Online Library on [11/11/2026]. See the Terms and Conditions (https://onlinelibrary.wiley.com/terms-and-conditions) on Wiley Online Library for rules of use; OA articles are governed by the applicable Creative Commons License

topography, Moho relief and temperature induced 3D variations in mantle seismic wave velocity. Our model is designed to investigate the global average Moho depth, constrain both the velocity and topography of individual crustal layers, and incorporate a 3D seismic velocity model of the upper mantle. To achieve this, it jointly incorporates Apollo seismic data, Lunar Orbiter Laser Altimeter (LOLA) topography, GRAIL gravity measurements, and thermodynamic equations of state. The integration of these complementary data sets enables a more robust and coherent understanding of the Moon's internal structure than with individual data sets.

The remainder of this paper is organized as follows. Section 2 describes the construction of our model, the simplified ray-tracing scheme, the data used in this study, and the parameterization of the inversion problem. Section 3 investigates the model's sensitivity to mantle velocity structure and the relief of the upper–lower crustal interface, and presents inversion results obtained without incorporating a 3D thermal mantle model. Section 4 presents inversion results that incorporate a mantle velocity model derived from a 3D thermal structure. Section 5 discusses the geological implications of the new results and offers concluding remarks.

2. Construction of the Lunar Crust and Upper Mantle Model

2.1. Modeling Hypotheses and Parameterization

Our model includes a three-layer crust beneath the Apollo stations, which consists of a subsurface low-velocity layer (LVL) (also referred to as the "large-scale ejecta layer"), a structurally disturbed upper anorthositic crust, and a fractured lower noritic crust (see Figure S1 in Supporting Information S1 for an overview, Jolliff et al., 2006). We assume that fractures extend into the upper mantle (Gillet et al., 2017; Lognonné et al., 2003) and therefore did not adopt a four-layer crust model (Nakamura, 1983). This assumption is supported by experiments on viscous deformation at elevated temperatures (Wieczorek et al., 2013) and aligns with the results of scattering studies (e.g., Gillet et al., 2017). The velocity of the ejecta layer is fixed to $V_p = 1$ km/s and $V_s = 0.5$ km/s, while the P-wave velocity and the average depths of the upper–lower crustal boundary and the Moho are treated as inverted model parameters (those are V_p^a, V_p^b, H^a, H^b; V_p denotes the P-wave velocity, H represents the average depth of each layer, a refers to the upper lunar crust, and b to the lower lunar crust). S-wave velocity in the crust is computed from P-wave velocity using a fixed ratio $V_s^{a,b} = V_p^{a,b}/\sqrt{3}$ (e.g., Lognonné et al., 2003; Nakamura, 1983).

To introduce surface topography, we use the global topographic map obtained by LOLA (Smith et al., 2010). Since there are no data that globally constrain the lateral variations of the ejecta layer (Chenet et al., 2006; Khan & Mosegaard, 2002), we assume that this layer is uniform and parallel to the surface with a constant thickness of 1 km. The structure of the upper–lower crust interface remains poorly constrained, and the currently available data do not permit reliable estimates of the interface depth beneath individual sites. Two simple assumptions regarding the interface can be made: (a) it is parallel to the surface (Figure 1a), (b) it is parallel to the Moho (Figure 1b, Wieczorek & Phillips, 1997). We will test both cases in Section 3.1.2. For the crust-mantle interface (i.e., the Moho), instead of inverting for crustal thickness (i.e., Moho depth) beneath each site separately (Chenet et al., 2006; Zhang et al., 2026), we invert for the average crustal thickness of the Moon instead and use gravity data to constrain the lateral variations in Moho depth. We use the selected average crustal thickness (H^b), average upper mantle density (ρ_m), and average crustal porosity (φ) to compute the lunar Moho map following the method in Wieczorek et al. (2013), which constructed a global crustal thickness model from GRAIL gravity and LOLA topography data in each iteration of our inversion. Please note that only H^b is the parameter we aim to invert; the assumptions for ρ_m and φ are determined by H^b. More detailed explanations of the calculation and assumptions are described in Supplement S2 in Supporting Information S1. In this context, our model does not introduce additional parameters compared to the 1D model.

According to the global Moho thickness map, the thickness of the lunar crust varies considerably from site to site (up to ~80 km). The limited thickness of the crust in some areas prevents the simultaneous representation of upper and lower crustal layers under our three-layer crust assumptions. In such thin-crust regions, we construct a two-layer crust by combining upper and lower crust (surface ejecta layer is still retained). An example of the thin crust setting can be seen at around 30° in Figure 1. To be more specific, for assumption (1), the upper crustal thickness is H^a (including 1 km ejecta layer), if the crustal thickness in some areas (H_i^b, i corresponding to a given site) is smaller than the upper crustal thickness ($H_i^b \leq H^a$), we use a two-layer crust in which the combined layer P-wave

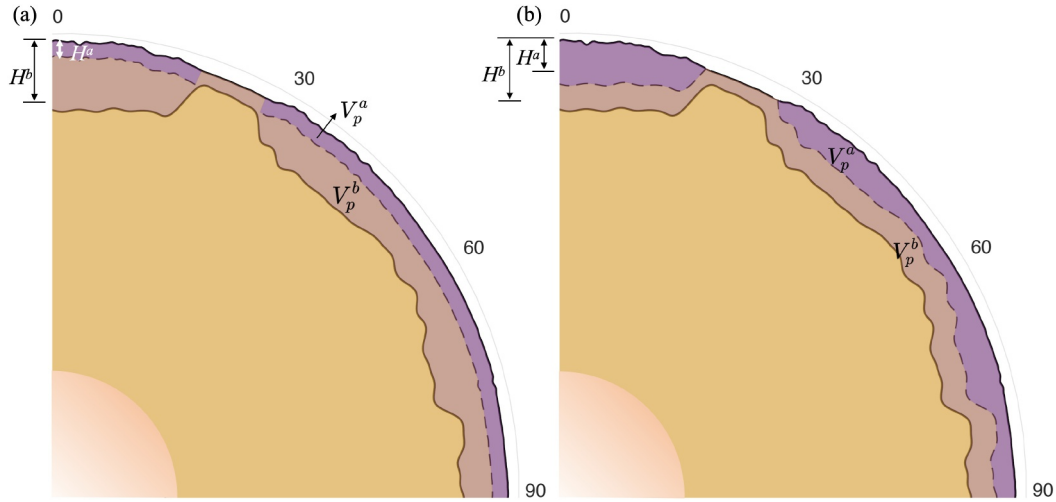

Figure 1. Schematic diagram of a cross-section of our model for different upper-lower crust interface assumption. (a) Shows assumption (1) that the interface is parallel to the surface, and (b) shows assumption (2) that the interface is parallel to the Moho. Layer thickness and topographic relief are magnified 5 times, respectively, but the ejecta layer is too thin to be visible here. The mantle velocity model is uniform here.

velocity is set to V_p^b. For assumption (2), upper crust thickness $H_i^a = H_i^b - \left(H^b - H^a\right)$, we use a two-layer crust with the combined layer *P*-wave velocity equal to V_p^b when $H_i^a \leq 1$ km (Figure 1). Notice that we treat the model this way for computational convenience. We prefer to use the *P*-wave velocity V_p^b to represent the combined layer, since such a region with thin crust is normally covered by a layer of mare basalts that exhibit high compressional wave velocity (Besserer et al., 2014; Gong et al., 2016). Therefore, the apparent mean velocity of this layer is expected to be closer to the lower crust, which has a higher velocity than the upper crust.

In the lunar mantle, we employ a 3D seismic wave velocity model derived from a combined thermal and thermodynamic approach. This model incorporates the previously introduced global Moho map and the same upper mantle density (ρ_m) and crustal porosity (φ) parameters, which are based on the average crustal thickness H^b. We describe the calculation of this model in the following section.

2.2. Computation of 3D Mantle Velocity Model

For a given average crustal thickness H^b, we use the corresponding Moho map and relevant parameters (ρ_m and φ) as input to compute the 3D thermal structure of the mantle.

Similar to other hybrid seismic-geodynamic inversion approaches (Drilleau et al., 2021; Magali et al., 2021), the approach exploits the link between the present-day 3D seismic structure of the Moon and its thermo-chemical structure. The latter is determined by the geometry and physical properties (such as density, thermal conductivity, and the heat production rate of radiogenic elements) of the Moon's various layers, including the crust and mantle. The core, however, is assumed to contain no radiogenic elements (Ziethe et al., 2009). The 3D thermal structure of the Moon stems from a heat balance model, under the assumption that the present-day Moon no longer experiences convection. This assumption is supported by the fact that the present-day Moon is relatively cold, especially for the elastic lithosphere extending to depths of 800–1,000 km, where deep moonquakes are located (Kawamura et al., 2017; Lognonné et al., 2003). This leads to Rayleigh number below the critical threshold for convection, as we describe in Supplement S2 in Supporting Information S1.

In this case, we can therefore solve for an energy conservation equation devoid of heat advection to obtain the 3D temperature field expressed below in spherical coordinates:

$$\rho(r,\theta,\phi)C_p\frac{\partial T(r,\theta,\phi)}{\partial t} = \nabla\cdot(k(r,\theta,\phi)\nabla T) + Q(r,\theta,\phi), \quad (1)$$

21699100, 2026, 11, Downloaded from https://agupubs.onlinelibrary.wiley.com/doi/10.1029/2026JE009866 by Okayama University, Wiley Online Library on [11/11/2026]. See the Terms and Conditions (https://onlinelibrary.wiley.com/terms-and-conditions) on Wiley Online Library for rules of use; OA articles are governed by the applicable Creative Commons License

Table 1
Comparison of Model Compositions Between Garcia et al. (2019) and This Study

	CaO	FeO	MgO	Al_2O_3	SiO_2	TiO_2	Na_2O
This study	3.09	9.33	36.36	3.91	47.26	–	0.05
Model M3	4–8	14–24	29–32	0–2	36–40	7–13	–

Note. All numbers are in wt %.

where C_p is the specific heat at constant pressure, T is the temperature, k is the thermal conductivity and Q is the radioactive heat source density. All these quantities vary in space (r, θ, ϕ) as a result of lateral variations on surface and the Moho topography.

The equation above can be further simplified by making the reasonable approximation that the diffusing Moon is at steady-state stage, leading to the following Poisson equation:

$$\nabla \cdot (k(r, \theta, \phi) \nabla T) = -Q(r, \theta, \phi). \tag{2}$$

Invoking the assumptions of non-convecting and steady-state Moon at the present-day not only considerably reduces the parameter space because no initial conditions are required, but also prevents us from prohibitive modeling the transient dynamics.

Once the temperature field is computed in the Cartesian domain, it is projected onto a spherical coordinate system, and, following Ziethe et al. (2009), the lithostatic pressure field in the mantle is approximated using the following analytical expression (Turcotte & Schubert, 2002):

$$P(r, \theta, \phi) = \frac{4}{3}\pi G \rho_m R_c^3 (\rho_c - \rho_m)\left(\frac{1}{r} - \frac{1}{R}\right) + \frac{2}{3}\pi G \rho_m^2 (R^2 - r^2) + P_{cr}(\theta, \phi), \tag{3}$$

where G is the gravitational constant and $\rho_c = 5{,}200\ \mathrm{kg/m^3}$ is the density of the core (Garcia et al., 2011). P_{cr} is the lithostatic pressure at the base of the crust, which is estimated as: $\rho_{cr}\ g\ D_{cr}(\theta, \phi)$. Note that here D_{cr} is the local crustal thickness, which varies laterally (hence $D_{cr}(\theta_i, \phi_i) = H_i^b$).

The grain density of the crust (solid mineral density without porosity) is the same as the average value in our gravity model ($2927.4\ \mathrm{kg/m^3}$, Wieczorek et al., 2013), and the bulk density of crust (ρ_{cr}) is computed according to the average crust porosity φ that we used in the gravity model. The density of mantle also use the same value as gravity model according to the average crustal thickness H^b. We fix the heat source density of the mantle to $4 \times 10^{-9}\ \mathrm{W/m^3}$ and mantle thermal conductivity k_m to 3 W/m/K (Ziethe et al., 2009). As the lunar mantle has a heat source density two orders of magnitude lower than the crust and a thermal conductivity one order of magnitude higher, its contribution to shaping the temperature profile is comparatively minor. The crustal heat source density (Q_{cr}) and thermal conductivity (k_{cr}) were varied as a function of the average crustal thickness H^b (similar to ρ_m and φ, Table S2 in Supporting Information S1).

Using the resulting temperature and pressure model, the 3D seismic wave velocity fields in the mantle were computed using the Gibbs free energy minimization code `Perple_X` (Connolly, 2005) assuming a mantle composition following Warren (2005) (Table 1). The values of Q_{cr} and k_{cr} were determined by requiring the resulting velocity model to be consistent with the Apollo seismic data (see Section 3.1 for details). As mentioned above, the seismic velocity field outside the mantle is prescribed but not computed here.

Rather than attempting to reconstruct the lunar mantle in full detail, we develop a simplified 3D lunar mantle velocity model to preliminarily investigate whether variations in Moho depth can produce measurable changes in mantle temperature and, consequently, seismic velocity. In this framework, lateral velocity variations are controlled by temperature variations induced by lateral changes in crustal thickness, and the resolution of these variations is therefore governed by the resolution of the thermal model rather than by the seismic data set. Here, the Apollo seismic data are used only as local anchor points for the 3D model.

21699100, 2026, 11, Downloaded from https://agupubs.onlinelibrary.wiley.com/doi/10.1029/2026JE009866 by Okayama University, Wiley Online Library on [11/11/2026]. See the Terms and Conditions (https://onlinelibrary.wiley.com/terms-and-conditions) on Wiley Online Library for rules of use; OA articles are governed by the applicable Creative Commons License

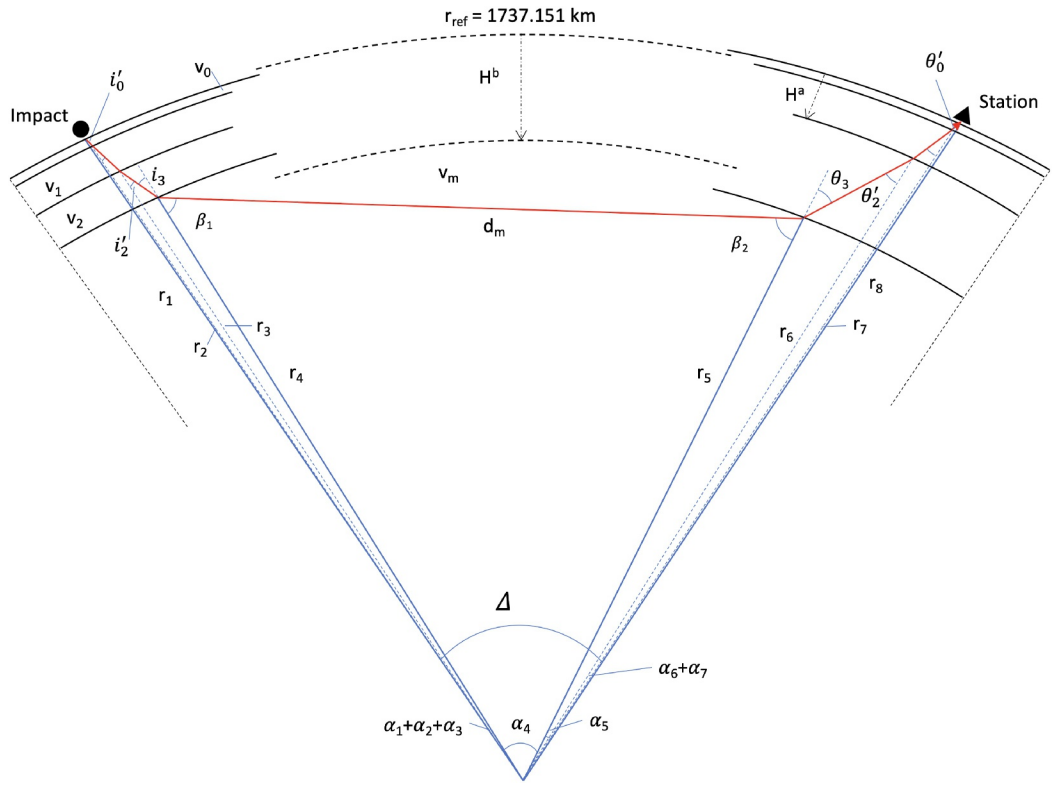

Figure 2. Schematic diagram of a Pn wave propagating through a lunar crustal model with laterally varying layer thickness. r is the radius of the boundary of each layer and v is the velocity of each layer. i' is a departing angle and i is an incident angle, while θ' is an incident angle to upward layer and θ means a departing angle in an upper layer. The sum of all the α angles equals Δ. Note that not all the angles were indicated in this figure. This diagram shown the case of upper-lower crust interface assumption (1).

2.3. Ray Tracing and Arrival Times Computation

Our forward modeling consists of computing synthetic body wave arrival times from a 3D lunar model. We first describe how to compute travel times in a 2D lunar crust model, which incorporates topographic relief and assumes laterally homogeneous velocities within each crustal layer, combined with an 1D average mantle velocity profile obtained by laterally averaging the 3D mantle velocity model. We then extend this approach to the case using a fully 3D mantle velocity model.

To optimize the efficiency of the calculations, we apply different methods to compute the ray paths and arrival times for events at varying epicentral distances. When the epicentral distance between an impact event and an Apollo station is less than 30°, the ray penetration depth is shallower than 90 km (Figure S8 in Supporting Information S1), and the 1D mantle velocity profile from the top of the mantle to this depth is nearly constant (see Section 3.1.1). In this case, we use Snell's law to compute the ray path and arrival time. As shown in Figure 2, we consider a three-layer crust and a constant uppermost mantle velocity. Based on Snell's law and the law of sines, a relationship can be derived between the epicentral distance Δ and the ray-path lengths in each layer. Since velocity is constant within each layer, the total travel time is obtained by summing the path length divided by the corresponding layer velocity over all layers. For other ray paths, such as waves propagating within the lunar crust, the travel-time calculation follows a similar approach (see Supplement S3 in Supporting Information S1 for calculation details). During the inversion, the travel times of waves with different phases along all possible paths are computed, and the minimum travel time is taken as the first-arrival time.

When the epicentral distance of an impact event from an Apollo station is greater than 30°, the first-arriving phase must be the mantle-traveling Pn wave. We use the `TauP` software (Crotwell et al., 1999) to compute ray paths and arrival times. Specifically, we calculate travel times for two separate 1D velocity models: one representing the structure beneath the seismic station and the other representing the structure beneath the impact site. The target

21699100, 2026, 11, Downloaded from https://agupubs.onlinelibrary.wiley.com/doi/10.1029/2026JE009866 by Okayama University, Wiley Online Library on [11/11/2026]. See the Terms and Conditions (https://onlinelibrary.wiley.com/terms-and-conditions) on Wiley Online Library for rules of use; OA articles are governed by the applicable Creative Commons License

21699100, 2026, 11, Downloaded from https://agupubs.onlinelibrary.wiley.com/doi/10.1029/2026JE009866 by Okayama University, Wiley Online Library on [11/11/2026]. See the Terms and Conditions (https://onlinelibrary.wiley.com/terms-and-conditions) on Wiley Online Library for rules of use; OA articles are governed by the applicable Creative Commons License

travel time is then taken as the average of the travel times predicted by these two models. This reduces computational cost while accounting for vertical velocity gradients in the mantle model, and tests show that the resulting errors are much smaller than the observational uncertainties (see Supplement S3 in Supporting Information S1 for details).

To incorporate a 3D mantle velocity model while ensuring sufficient computational efficiency for implementation within a Bayesian framework, we adopt a two-step approach. We first compute the ray path between the source and the station using the 1D average profile of the 3D mantle velocity model. Then we freeze the ray path and compute the travel time along this path, taking into account the 3D velocity variations within the mantle. Fixing the ray paths to compute travel times in the 3D mantle greatly improves computational efficiency. This approximation is feasible based on Fermat's principle: perturbing the actual trajectory to a simplified path influences the time integral only to second order (Nolet, 2008).

Please note that our seismic modeling approach is highly simplified compared with fully 3D modeling approaches. It extends the 1D model by incorporating lateral variations in crustal layer thickness, but does not account for lateral variations in density, porosity, or seismic velocity within individual layers. In addition, it neglects interface tilting and 3D refraction effects. Therefore, the ray tracing is performed in a 2D framework. Given the limitations of currently available Apollo seismic data, constraining such lateral heterogeneity in seismic velocities is not realistic. Gravity data can provide constraints on lateral variations in density and porosity; however, it is relatively insensitive in nearside mare regions (Wieczorek et al., 2013). These simplifications mean that the gravity model neglects the comparatively thin surficial layer of dense basalt in mare regions, which may introduce localized biases in crustal thickness estimates, although these are unlikely to exceed a few kilometers (Wieczorek et al., 2013). Furthermore, although gravity data can resolve wavelengths as short as 26 km, shorter-wavelength structural variations may still introduce discrepancies between true crustal thickness at local scales and gravity-derived estimates. Collectively, these limitations highlight the discrepancy between the inherent complexity of the true 3D interior structure and the constraints imposed by current data sets. Nevertheless, our analysis represents a preliminary attempt to extend the framework from a 1D to a quasi-3D representation, and more refined modeling must await the acquisition of additional and more comprehensive data sets. To evaluate the potential impacts of the model simplifications, we will further assess the robustness of our method in subsequent analyses (see Section 3.2).

2.4. Inverse Problem and Prior Information

We apply the same Bayesian approach described in Zhang et al. (2026) to solve the inverse problem by retrieving model parameters from seismic wave arrival times. Here, we define the upper-/lower-crust velocities, along with the average upper mantle velocity as the first-order velocity structure, and consider both the vertical and lateral variations in upper mantle velocity as second-order structures. In the framework of a 2D lunar crust model combined with an average 1D mantle velocity profile, we invert for the seismic velocities (V_p^a, V_p^b, V_p^m) and average thicknesses of the crustal layers (H^a, H^b). Lateral variations of each crustal boundary are constrained by gravity and topography data, whereas vertical variations in mantle velocity are governed by a thermodynamic model; thus, only the average upper-mantle velocity is inverted for. Note that lateral variations in mantle velocity are not included here. In the case where the model is coupled with a fully 3D mantle velocity model, lateral variations in mantle velocity are taken into account, but the average velocity of the upper mantle is kept fixed owing to computational cost constraints.

Table 2 shows the prior model parameter information. The inversion includes a total of 7 artificial impacts and 8 meteoroid impacts, with 42 *P*-wave arrival times (14 from artificial events) and 3 *S*-wave arrival times (Tables S4–S6 in Supporting Information S1, Zhang et al., 2026). We determined the velocity range for the inversion based on Garcia et al. (2019), which summarized most of the published models. There is no adequate evidence to constrain the average depth of the upper-lower crust interface; it is distributed between 10 and 25 km in previous studies (Table S3 in Supporting Information S1). Therefore, we use a range from 1 to 25 km for H^a. The Moho depth is distributed between 29 and 65 km in previous studies (Table S3 in Supporting Information S1), and recent studies prefer a thinner crust that corresponds to a global average crustal thickness (H^b) from 34 to 50 km (Supplement S4 in Supporting Information S1). To adequately account for uncertainties, we consider the range for H^b from 25 to 60 km. We use the uppermost mantle velocity V_p^m to represent the *P*-wave velocity profile of the

21699100, 2026, 11, Downloaded from https://agupubs.onlinelibrary.wiley.com/doi/10.1029/2026JE009866 by Okayama University, Wiley Online Library on [11/11/2026]. See the Terms and Conditions (https://onlinelibrary.wiley.com/terms-and-conditions) on Wiley Online Library for rules of use; OA articles are governed by the applicable Creative Commons License

Table 2
The Prior Model Information of Inverted Parameters

Description	Quantity	Value/Range
P-wave velocity of the upper crust V_p^a $\left(V_s^a = V_p^a/\sqrt{3}\right)$	1	2–6 km/s
P-wave velocity of the lower crust V_p^b $\left(V_s^b = V_p^b/\sqrt{3}\right)$	1	4–7.3 km/s
P-wave velocity of the uppermost mantle V_p^m $\left(V_s^m = V_p^m/\sqrt{3}\right)$	1	7–9 km/s
Average depth of upper crust H^a	1	1–25 km
Average depth of crust H^b	1	25–60 km
Latitude of meteoroid impact	8	−90–90°
Longitude of meteoroid impact	8	−180–180°

Note. The "Quantity" in the middle column represents the number of each parameter.

mantle, while its depth-dependent variations are constrained by the thermodynamic model. For the locations of the meteoroid impact events, longitudes range from −180° to 180°, and latitudes range from −90° to 90°. The depths of all impact events are set to zero. It should be noted that the upper mantle density ρ_m and crustal porosity φ, as well as the crustal heat source density Q_{cr} and thermal conductivity k_{cr}, were predetermined during the tests to match the average crustal thickness H^b, rather than treated as independent inversion parameters. The prior ranges for the crustal heat source density Q_{cr} and thermal conductivity k_{cr} are based on Ziethe et al. (2009) (Table S2 in Supporting Information S1).

The misfit function employed in the seismic inversion is defined as:

$$S(\mathbf{d},\mathbf{m}) = \sum_{i=1}^{N}\sum_{j=1}^{4}\frac{\left(t_{p_{ij}}^{\mathrm{cal}}(\mathbf{m}) - t_{p_{ij}}^{\mathrm{obs}}\right)^2}{\sigma_{p_{ij}}^2} + \sum_{i=1}^{M}\sum_{j=1}^{4}\left(\frac{\left(\left(t_{p_{ij}}^{\mathrm{cal}}(\mathbf{m}) - t_{\mathrm{ref}p_i}^{\mathrm{cal}}(\mathbf{m})\right) - \left(t_{p_{ij}}^{\mathrm{obs}} - t_{\mathrm{ref}p_i}^{\mathrm{obs}}\right)\right)^2}{\left(\sigma_{p_{ij}} + \sigma_{\mathrm{ref}p_i}\right)^2} + \frac{\left(\left(t_{s_{ij}}^{\mathrm{cal}}(\mathbf{m}) - t_{p_{ij}}^{\mathrm{cal}}(\mathbf{m})\right) - \left(t_{s_{ij}}^{\mathrm{obs}} - t_{p_{ij}}^{\mathrm{obs}}\right)\right)^2}{\left(\sigma_{s_{ij}} + \sigma_{p_{ij}}\right)^2}\right), \tag{4}$$

where i represents different events. N and M denote the numbers of artificial and meteoroid impacts, respectively; the former have known occurrence times, while the latter do not. j represents different Apollo stations, and σ is the standard deviation of the error associated with each arrival time. t_p^{cal} and t_p^{obs} represent synthetic and observed *P*-wave travel times, respectively. $t_{\mathrm{ref}p}$ is the reference *P*-wave arrival time recorded by one of the four stations for each meteoroid impact event, which is used to compute differential arrival times at different stations. Specifically, $t_{\mathrm{ref}p_i}^{\mathrm{obs}}$ represents the observed arrival time of the reference *P*-wave for the ith event. The differential arrival time of the *S* wave is referenced to the *P*-wave arrival time at the same station.

3. Inversion Tests With an 1D Average Mantle Velocity Model

3.1. Mantle Velocity Model and Upper-Lower Crust Interface Assumption Test

3.1.1. Sensitivity to the Mantle Velocity Model

We first tested the sensitivity of the seismic data set to vertical variations in mantle velocity. By evaluating how well the average velocity profile of the 3D mantle velocity model matches the seismic data, we aim at determining the corresponding thermodynamic parameters and at verifying our compositional hypothesis of the Moon. Another velocity model derived from a 1D thermal model (M3) and a velocity model derived from seismic data (M2), both published in Garcia et al. (2019), were also tested for comparison. Figure 3a shows a typical average profile of our 3D mantle velocity model (laterally averaged for the nearside hemisphere, red curve), which has an almost constant velocity from the top of the mantle to about 100 km depth. At depths of 100–140 km we observed a velocity interface that is caused by a phase transition, this is also seen in model M3 in Garcia et al. (2019), but for model M2 in Garcia et al. (2019), there is a slight velocity reduction at this depth. Then, the velocity in our model

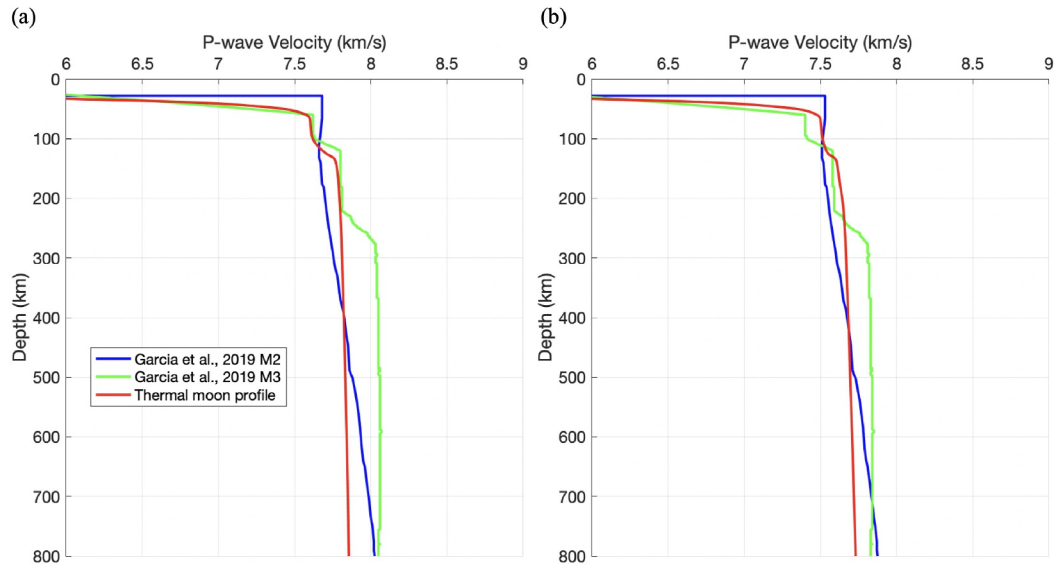

Figure 3. (a) Laterally averaged *P*-wave velocity profile of our 3D thermal mantle velocity model (red) and 1D velocity models M2 (derived from seismic data, blue), M3 (derived from 1D thermal model, green) from Garcia et al. (2019). The red curve corresponds to the model with $H^b = 35$ km, $Q_{cr} = 320 \times 10^{-9}$ W/m^3 and $k_{cr} = 0.60$ W/m· K, yielding an uppermost mantle velocity of approximately 7.6 km/s. (b) Velocity models of M2 and M3 with the applied offsets, together with the optimized reference profile obtained from our parameter tests. The reference profile corresponds to the model with $H^b = 35$ km, $Q_{cr} = 480 \times 10^{-9}$ W/m^3 and $k_{cr} = 0.42$ W/m· K, yielding an uppermost mantle velocity of approximately 7.5 km/s. Additional 1D velocity profiles for different parameter combinations are provided in Supplement S2 in Supporting Information S1.

will only slightly increase with depth. In model M3, there is another interface below 200 km depth, which is absent in our model. This is mainly due to the different composition assumptions between these two models (Table 1), because composition in particular can affect phase proportions and the depth at which the phase change occurs.

The main parameters of our thermal model, heat source density (Q_{cr}) and thermal conductivity (k_{cr}) in the crust, will generally influence the magnitude of the velocity profile, but will not change its global trend significantly (Figure 3). We fit the average mantle velocity profile to the seismic data by varying the average crustal thickness H^b and the parameters k_{cr} and Q_{cr}, and we then determined the optimal values of k_{cr} and Q_{cr} for each value of H^b (Table S2, Figure S3 in Supporting Information S1). According to the inversion, an uppermost mantle velocity of 7.5 ± 0.04 km/s provides the best fit within the data uncertainties (Figure 4). The red curve in Figure 3b shows the mantle *P*-wave velocity profile with an uppermost mantle velocity of $V_p^m = 7.5$ km/s, which we adopt as the reference profile for constructing the 3D thermal velocity model in the subsequent analysis.

When the M2 and M3 mantle velocity models of Garcia et al. (2019) are applied to the same seismic data set, the resulting misfit values are clearly larger than those from our model (Figure S12 in Supporting Information S1), primarily due to their higher average *P*-wave velocities. In order to eliminate the impact of the average velocity while assessing the effect of vertical variations in mantle velocity, an offset parameter dv was applied to the M2 and M3 models of Garcia et al. (2019) for comparison. The resulting *P*-wave velocities at the top of the mantle for models M2 and M3 are 7.53 ± 0.04 km/s and 7.47 ± 0.04 km/s, respectively (Figure 3b). Models M2 and M3 show a slower velocity than previous results, and we will explain this further below.

We evaluated the sensitivity of the Apollo seismic data to vertical variations in the mantle velocity model by comparing misfit values during the tests. Figure 5 shows the test results for three models. We did not see an obvious difference between model M2 and our average thermal velocity profile, while they both fit the Apollo seismic data slightly better than model M3. This result indicates that the current seismic data set is primarily sensitive to the first-order velocity structure of the lunar mantle, but not sufficiently sensitive to the second-order variations in velocity with depth. Furthermore, it should be noted that the sensitivity of seismic data to first-order velocity structure is itself limited to the lunar nearside, specifically the region covered by the Apollo seismic stations and impact sites, rather than being globally representative. In this sense, it provides only a localized

21699100, 2026, 11, Downloaded from https://agupubs.onlinelibrary.wiley.com/doi/10.1029/2026JE009866 by Okayama University, Wiley Online Library on [11/11/2026]. See the Terms and Conditions (https://onlinelibrary.wiley.com/terms-and-conditions) on Wiley Online Library for rules of use; OA articles are governed by the applicable Creative Commons License

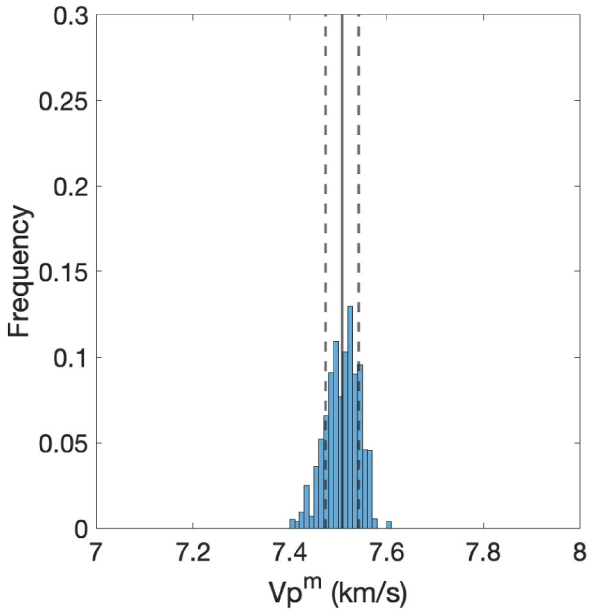

Figure 4. Output marginal distributions of the uppermost mantle *P*-wave velocity. Black line is mean and dashed lines are 1-σ of the output values.

anchor for the global 3D model, whereas the global mantle velocity structure, as well as the lateral variations in lunar crustal thickness, are constrained by thermal models and high-resolution gravity data, respectively.

In Figure 6 we show two-dimensional marginal distributions to depict the correlation between the uppermost mantle velocity V_p^m and the average Moho depth H^b for different models. Although these models differ somewhat in their second-order structures, they yield similar results for the Moho depth, given their comparable first-order velocity magnitudes. Since the average profile (Figure 3b, red curve) of our 3D mantle velocity model fits the seismic data as well as, or even better than, the other two models, and since different vertical variation models do not significantly affect the Moho depth inversion results under appropriate first-order (average) mantle velocity magnitudes, it is reasonable to employ it as a reference model for constructing our 3D mantle velocity models, which are primarily designed to constrain the lateral variations in uppermost mantle velocity.

3.1.2. Sensitivity to the Upper-Lower Crust Interface Assumption

We also tested the difference between our two assumptions about the upper-lower crust interface in Section 2.1. Assumption (1) shows a better fit to the data than assumption (2) (Figure 7). The difference between the two assumptions lies mainly in the different propagation paths of the rays. For assumption (2), the variations of the upper crustal thickness are larger than those of assumption (1), which leads to more rays propagating only in the upper crust. The better fit with the Apollo seismic data under assumption (1) suggests that the relief of upper-lower crust interface may not be as large as that of the Moho. However, this does not imply that the upper crustal thickness should be constant. Given the limited observations of the crustal interior, we choose assumption (1) in our inversions, and we believe that the current data set lacks the resolution necessary to accurately constrain the lateral variations of the upper-lower crustal interface.

If the upper-lower crust discontinuity is indeed related to the closure of fractures caused by lithostatic pressure (Simmons et al., 1973), then the depth of this interface is more likely to be associated with the surface topography. However, we cannot ignore the role of meteoroid impacts in altering the lunar upper crust. One possible scenario is that the fluctuation of the interface lies somewhere between those of the Moho and the surface topography (Onodera et al., 2021, 2022). In this study, we adopt assumption (1) to minimize potential ray-tracing deviations caused by an overestimation of upper-crustal depth variations.

Furthermore, possible lateral variations in the thickness and seismic velocities of the subsurface LVL may also affect the inversion results. Our tests show that varying the LVL thickness by ±0.5 km (i.e., from 0.5 to 1.5 km) produces a maximum *P*-wave travel-time difference of 1 s. This difference is comparable to the best available uncertainty in arrival-time measurements and could result in variations of approximately ±1.7 km in the estimated crustal thickness.

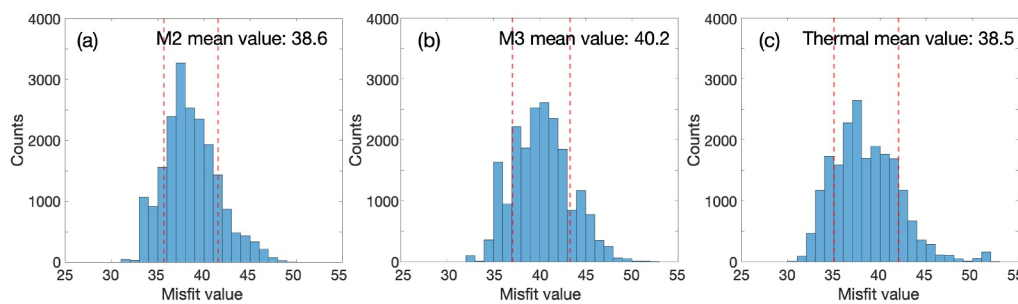

Figure 5. Misfit values for different mantle velocity models. Dashed red lines are 1-σ of the misfit values. Model name and corresponding mean misfit value is written in text on the panel. A total of 45 data points were used.

21699100, 2026, 11, Downloaded from https://agupubs.onlinelibrary.wiley.com/doi/10.1029/2026JE009866 by Okayama University, Wiley Online Library on [11/11/2026]. See the Terms and Conditions (https://onlinelibrary.wiley.com/terms-and-conditions) on Wiley Online Library for rules of use; OA articles are governed by the applicable Creative Commons License

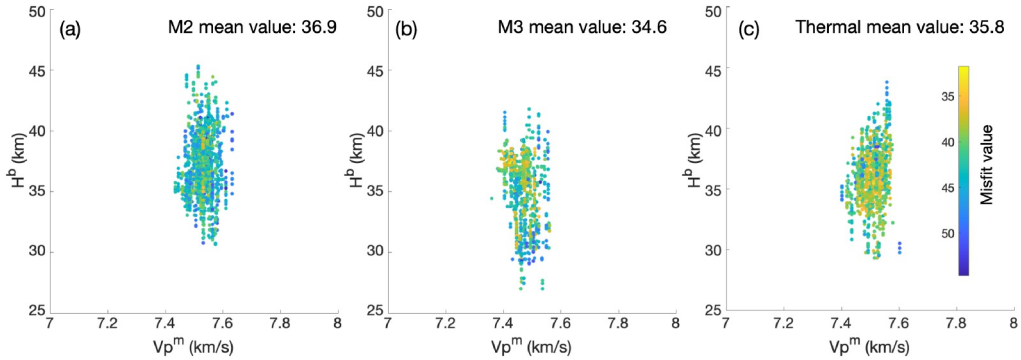

Figure 6. Correlations between Moho depth and upper mantle velocity for different mantle velocity models. Each panel shows the accepted values during the inversion. Model name and corresponding mean H^b value is written in text on the panel. Yellow and blue colors indicate small and large misfit values, respectively. Please note that some points may overlap.

3.2. Inversion Results

Here, we present inversion results based on a 2D lunar crust model combined with an average mantle velocity profile. We use assumption (1) for the upper-lower crust interface here.

Figure 8 shows the marginal distributions of the velocity and thickness of each layer of the lunar crust. The mean value of the average crustal thickness H^b is 35.8 ± 2.2 km, the corresponding lower crust velocity V_p^b is 6.4 ± 0.3 km/s. They are distributed within a limited range and we observed a minimized misfit value when H^b is around 36 km (Figure S13 in Supporting Information S1). For the average upper crustal depth H^a, accepted values range from 5 to 20 km, and V_p^a ranges from 2 to 4 km/s. The corresponding mean values and 1-σ uncertainties are $H^a = 12.1 \pm 3.2$ km and $V_p^a = 3.2 \pm 0.5$ km/s. The output P-wave velocity at the top of the mantle is 7.50 ± 0.04 km/s (Figure 4).

Figure 9 shows the correlations between depths and P-wave velocities of different layers. The acceptable ranges of upper crustal velocity and thickness are relatively large, while those for the lower crust and mantle are smaller. We can see a clear trade-off between V_p^a and H^a, as well as between V_p^b and H^a, while the trade-offs are less apparent for other parameters. Figure 10 displays all models accepted during inversion. The red profiles represent models with the best 10% of acceptable misfits. The black profile is the best-fit model (smallest misfit value).

The ray tracing results can help us explain the inversion results presented here. In Figure 11, we display the ray tracing results for the best-fit model shown in Figure 10. We can observe differences in the propagation paths of first-arrival P-waves depending on the crustal thickness variations between stations and impact sites. The light

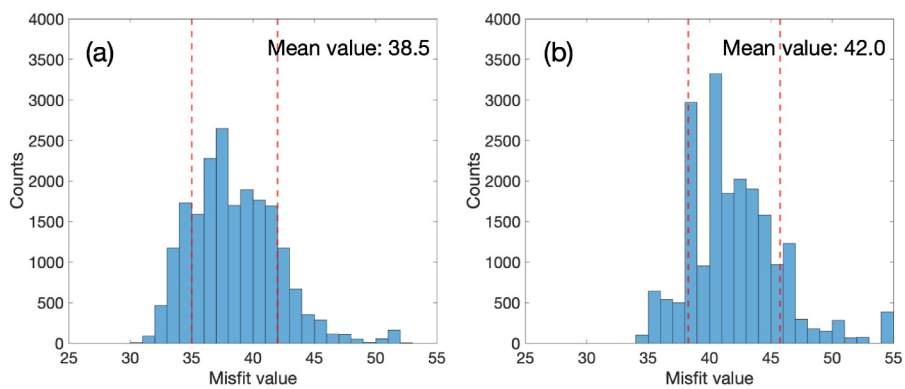

Figure 7. Misfit values for different mid-crust assumptions. Dashed red lines are 1-σ of the misfit values. (a) Is for assumption (1) and (b) is for assumption (2).

21699100, 2026, 11, Downloaded from https://agupubs.onlinelibrary.wiley.com/doi/10.1029/2026JE009866 by Okayama University, Wiley Online Library on [11/11/2026]. See the Terms and Conditions (https://onlinelibrary.wiley.com/terms-and-conditions) on Wiley Online Library for rules of use; OA articles are governed by the applicable Creative Commons License

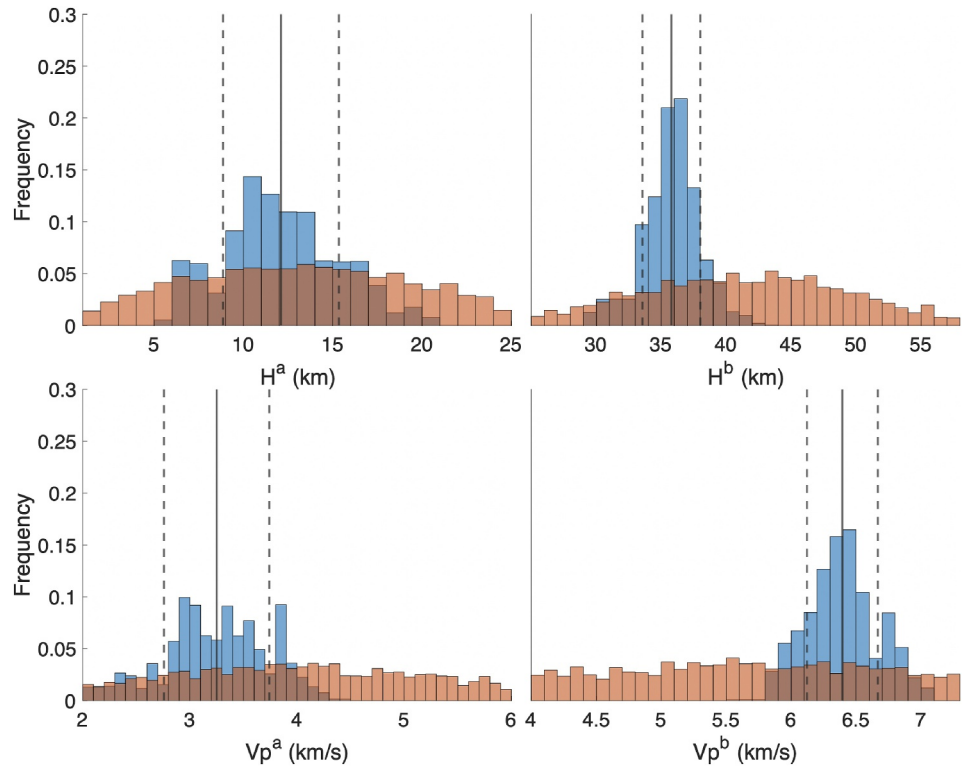

Figure 8. Marginal distributions of the inverted parameters in the crust. The orange and blue histograms correspond to the *a priori* and *a posteriori* distributions, respectively. Black lines are mean and dashed lines are 1-σ of the output values of each parameter.

blue dots represent rays that propagated only through the crust, while the red dots indicate rays that traveled into the mantle for first-arrival *P*-waves. In total, 42 *P*-wave arrival times were used in the inversion. Among these, 9 rays propagated within the crust: 1 ray traveled through the upper crust (14 LM recorded by Station 14) and 8 rays traveled through the lower crust. In addition, 2 of 3 *S*-waves propagated in the crust.

However, in the case of a 1D model, only a single ray propagates within the crust (Figure 11b). Compared to 1D models, considering lateral variations in lunar crustal thickness reveals that more first-arrival waves propagate through the crust (Figure 11). This new evidence is crucial, as previous studies failed to provide reliable constraints on crustal thickness from first-arrival data, primarily because they could not resolve the trade-offs between crustal thickness, mantle velocity, and the velocities of crustal layers. The new ray-tracing results offer additional observations of the lunar crust and help resolve the trade-offs between lower crust velocity (V_p^b), mantle velocity (V_p^m), and crustal thickness (H^b). We show above that the lower crust is better constrained than the upper crust, because the lower crust is better sampled (8 rays) than the upper crust (1 ray). Although all nine rays penetrated the upper crust, they cannot resolve the trade-off between H^a and V_p^a.

Besides, in previous studies (e.g., Khan et al., 2000; Lognonné et al., 2003; Gagnepain-Beyneix et al., 2006) which assumed a 1D crustal model, eight of the nine rays were thought to travel through the shallow mantle, and their travel times were used, along with other data, to invert for the upper mantle velocity. This could be one of the reasons why higher uppermost mantle velocities were observed in previous studies. Garcia et al. (2019) reported the presence of a LVL in the upper mantle based on seismic data (M1, M2), which is not consistent with thermal models (M3 and this study). Our tests indicate that the current resolution of lunar seismic data remains insufficient to confirm or rule out the presence of an LVL (Figure 5). The apparent LVL may instead represent an artifact arising from inaccurate ray tracing.

In addition, our model inevitably involves several simplifications that may introduce potential artifacts or biases into the ray-tracing results. To assess the robustness of our approach, we performed an additional inversion

21699100, 2026, 11, Downloaded from https://agupubs.onlinelibrary.wiley.com/doi/10.1029/2026JE009866 by Okayama University, Wiley Online Library on [11/11/2026]. See the Terms and Conditions (https://onlinelibrary.wiley.com/terms-and-conditions) on Wiley Online Library for rules of use; OA articles are governed by the applicable Creative Commons License

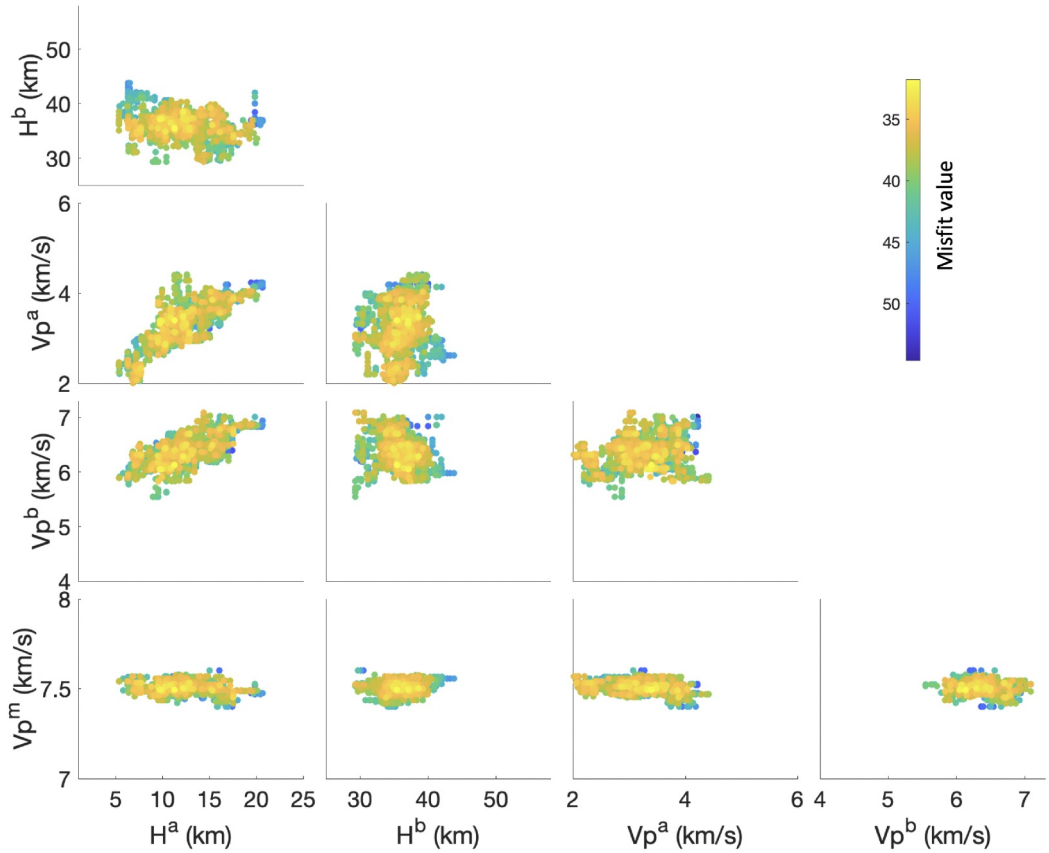

Figure 9. Correlations between the average depth and the *P*-wave velocity of each layer, for all the models accepted during the inversion. Yellow and blue colors indicate small and large misfit values, respectively. See also Figure S14 in Supporting Information S1 for the sampled frequencies of each pair of parameters.

excluding three of the eight rays propagating through the lower crust to account for uncertainties associated with these ray paths. The resulting model exhibits only minor differences (Figures S16 and S17 in Supporting Information S1), suggesting that our conclusions are not significantly affected by these uncertainties.

The data fit between all observed and computed arrival times for the 7 artificial impacts and 8 meteoroid impacts is shown in Figure 12 and Figure S18 in Supporting Information S1. Most of the models accepted by the algorithm can fit the observational data within the error bars. Artificial impacts represent better fits than meteoroid impacts. Although several picks show discrepancies larger than the expected error bars, none exceed 10 s, representing an improvement over previous models (Figure S18 in Supporting Information S1).

4. Inversion Results With a 3D Mantle Velocity Model

In this section, we extend our inversion approach by incorporating a 3D mantle velocity model. Introducing a 3D mantle velocity model shows a better data fit compared to 1D mantle velocity models (Figure 13). The new inversion results are presented in Figures 14–16 and Supplement S6 in Supporting Information S1, yielding mean values of $V_p^b = 6.5(\pm 0.3)$ km/s and $H^b = 35.1(\pm 2.6)$ km. These results are similar to those obtained from the 1D average mantle velocity profile, and the average crustal thickness is slightly thinner. The upper crust is also not constrained as well as the lower crust, as shown in Figure 14. Figure 15 show the correlations between different parameters. H^a and V_p^a exhibit relatively large uncertainties, as in Section 3.2, and show an apparent trade-off.

The average *P*-wave velocity in the uppermost mantle (V_p^m), as derived from the 3D mantle velocity model, is 7.50 km/s. Figure S23 in Supporting Information S1 presents the best-fitting 3D mantle velocity model from our

21699100, 2026, 11, Downloaded from https://agupubs.onlinelibrary.wiley.com/doi/10.1029/2026JE009866 by Okayama University, Wiley Online Library on [11/11/2026]. See the Terms and Conditions (https://onlinelibrary.wiley.com/terms-and-conditions) on Wiley Online Library for rules of use; OA articles are governed by the applicable Creative Commons License

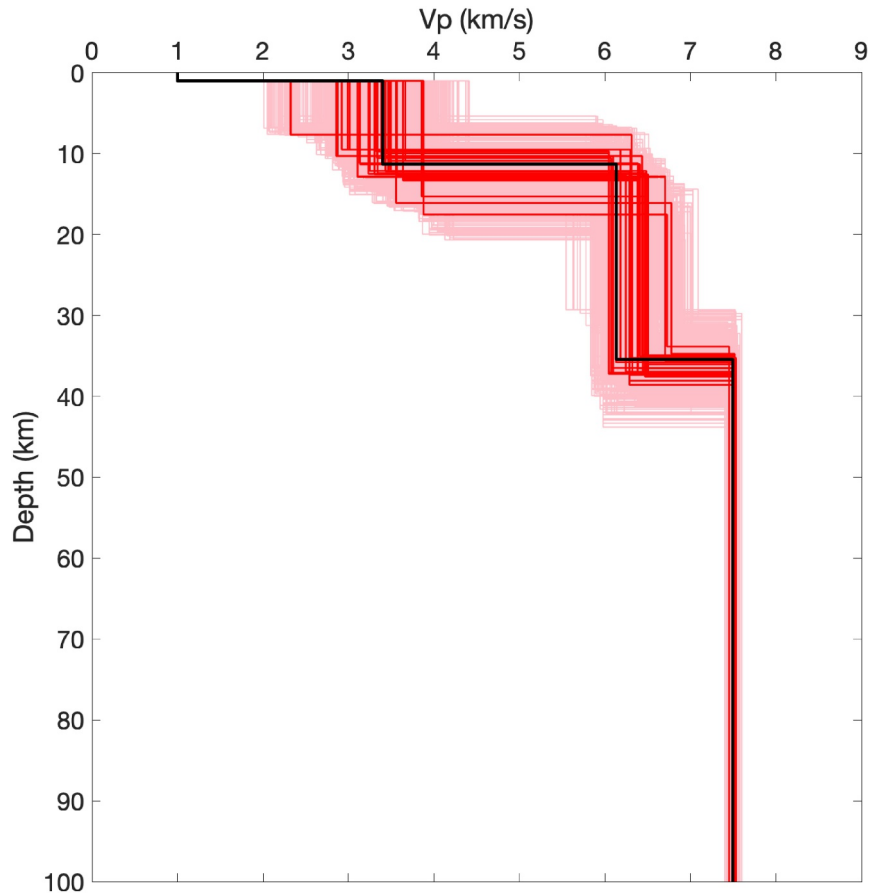

Figure 10. Inversion results for all accepted models. The red profiles represent models with the best 10% of acceptable misfits. The black profile indicates the best-fit model with the smallest misfit value. The velocity of the mantle corresponds to the velocity at the top of the mantle. Figure S15 in Supporting Information S1 shows the probability density functions of the *P*-wave velocities.

inversion. The lateral velocity variation in the nearside uppermost mantle reaches 0.7 km/s, ranging from 7.3 to 8.0 km/s. This results in a theoretical maximum travel time compensation of up to ±4 s and provides a better fit to the data compared to the average mantle velocity profile used in the previous section. An example showing a better fit is the artificial impact event SIVB 16 that was recorded by Station 15 (Figure 17). Not all ray paths are significantly affected, such as in regions where variations in crustal thickness are negligible, or for rays that do not pass through the mantle.

The integration of thermodynamic modeling with seismic data provides evidence for lateral variations in seismic wave velocities in the upper lunar mantle, which are attributed to variations in crustal thickness. However, it should be noted that our 3D thermal model primarily considers the effect of lateral variations in crustal thickness on upper mantle seismic velocities. It does not account for possible lateral heterogeneities in the distribution of heat-producing elements within the crust and mantle, nor for spatial variations in thermal properties and density, which may also influence the gravity-derived crustal thickness model (Che et al., 2025; Laneuville et al., 2013, 2018). Future integration of lateral variations in heat-producing elements and density into models is expected to provide a more accurate representation of lateral variations in seismic velocity structure.

The uppermost mantle velocity in this study is slightly lower than in previous studies (Figure 18b), mainly due to improved ray-tracing results. This value is also lower than *P*-wave velocities beneath the terrestrial Moho, which Steinhart (1967) defined as the transition to mantle material where seismic velocities show a steep increase to 7.6–8.6 km/s. Although we tested only one set of mantle compositional parameters in this study, the phase

21699100, 2026, 11, Downloaded from https://agupubs.onlinelibrary.wiley.com/doi/10.1029/2026JE009866 by Okayama University, Wiley Online Library on [11/11/2026]. See the Terms and Conditions (https://onlinelibrary.wiley.com/terms-and-conditions) on Wiley Online Library for rules of use; OA articles are governed by the applicable Creative Commons License

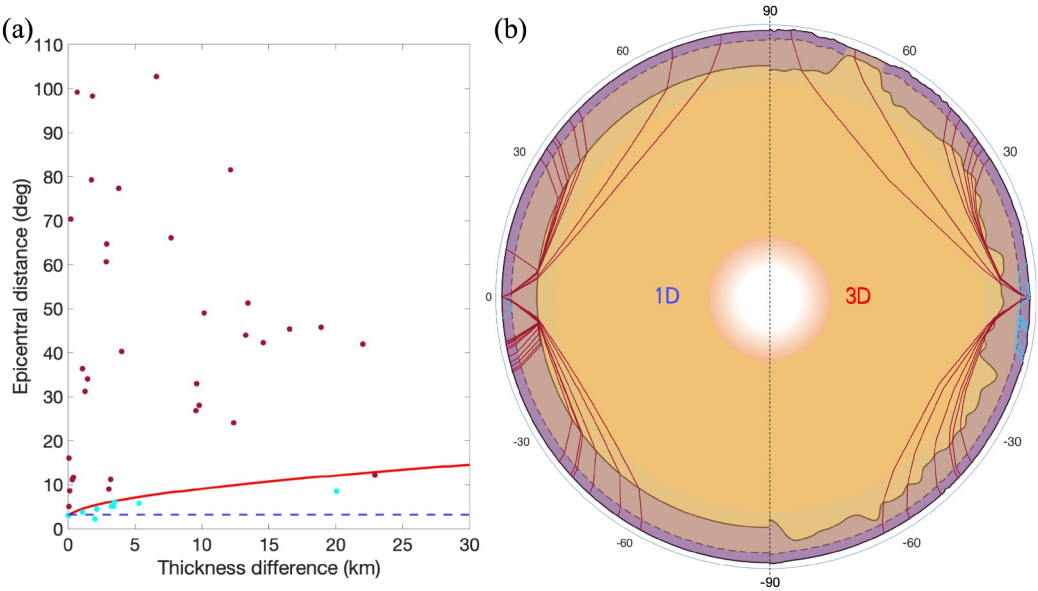

Figure 11. (a) Comparison of critical distances between the 1D and 2D models. The *X*-axis represents the absolute crustal thickness differences between the impact sites and the stations. The dashed blue line shows the critical distances at which the first arrivals begin to come from the mantle for a 1D model. The red line indicates the critical distances at which the first arrivals begin to come from the mantle for a 2D model. Dark red dots are arrivals come from the mantle and light blue dots are arrivals come from the crust for the 2D model. Note that the red line represents only a marginal dependence on the crustal thickness difference (with the same surface topography) and should not be used as an accurate basis for determining the ray's path for all the events. (b) Schematic diagram of *P*-wave ray paths in 1D and 2D models. Light blue lines show the rays propagating in the crust and dark red lines show the rays propagating in the mantle. The model on the right shows a cross-sectional view of the 3D Moon, with the ray paths projected onto this section and plotted for a single station. The ray paths are shown schematically to represent the range of epicentral distances and do not necessarily follow the actual topography along each path. For clarity, only a subset of the mantle-propagating ray paths is shown. Crustal thickness and topographic relief are magnified 5 times. The 3D mantle velocity variations are not shown here.

composition analysis indicates that pyroxenes account for more than 50% of the upper mantle. This may represent a real feature of the upper lunar mantle, as suggested by the relatively low *P*-wave velocity together with observations from the South Pole–Aitken (SPA) basin ejecta, which are dominated by low-calcium pyroxene (Melosh et al., 2017). As the largest impact basin on the Moon, the SPA is expected to have excavated and exposed mantle material (Andrews-Hanna et al., 2025; Potter et al., 2012). Our results imply that the lunar upper mantle may indeed be pyroxene-rich, rather than being dominated by olivine as in the Earth's mantle (O'Neill, 2005). Furthermore, phase composition analysis suggests that the increase in seismic velocity observed at approximately 100 km depth results from the appearance of spinel.

Figure 18a shows the 1D crustal velocity profiles of the lunar nearside. Our new crustal thickness estimates fall within the range of previous studies and are slightly greater than those reported in Lognonné et al. (2003). The derived lunar crustal velocity model represents the apparent velocity within the fractured lunar crust, in which pervasive fractures generate intense seismic scattering (Blanchette-Guertin et al., 2012; Gillet et al., 2017). This treatment of apparent velocity is consistent with the approach adopted in previous studies based on 1D models, and the resulting velocities agree well with previously published ranges.

5. Discussion and Conclusions

Based on a crustal thickness of 35 km, the average bulk crustal density obtained from GRAIL data is 2635 kg/m^3 (Table S1 in Supporting Information S1). Then, we estimated the crustal porosity using independent estimates of the crustal grain density (average 2927.4 kg/m^3, Wieczorek et al., 2013), which has been empirically correlated with the abundance of FeO and TiO_2 based on measurements across a wide range of lunar rock compositions (Huang & Wieczorek, 2012; Wieczorek et al., 2013). If we assume a constant porosity throughout the entire crust, the average crustal porosity is 10 ± 1% (Table S1 in Supporting Information S1). With a fixed crustal grain

21699100, 2026, 11, Downloaded from https://agupubs.onlinelibrary.wiley.com/doi/10.1029/2026JE009866 by Okayama University, Wiley Online Library on [11/11/2026]. See the Terms and Conditions (https://onlinelibrary.wiley.com/terms-and-conditions) on Wiley Online Library for rules of use; OA articles are governed by the applicable Creative Commons License

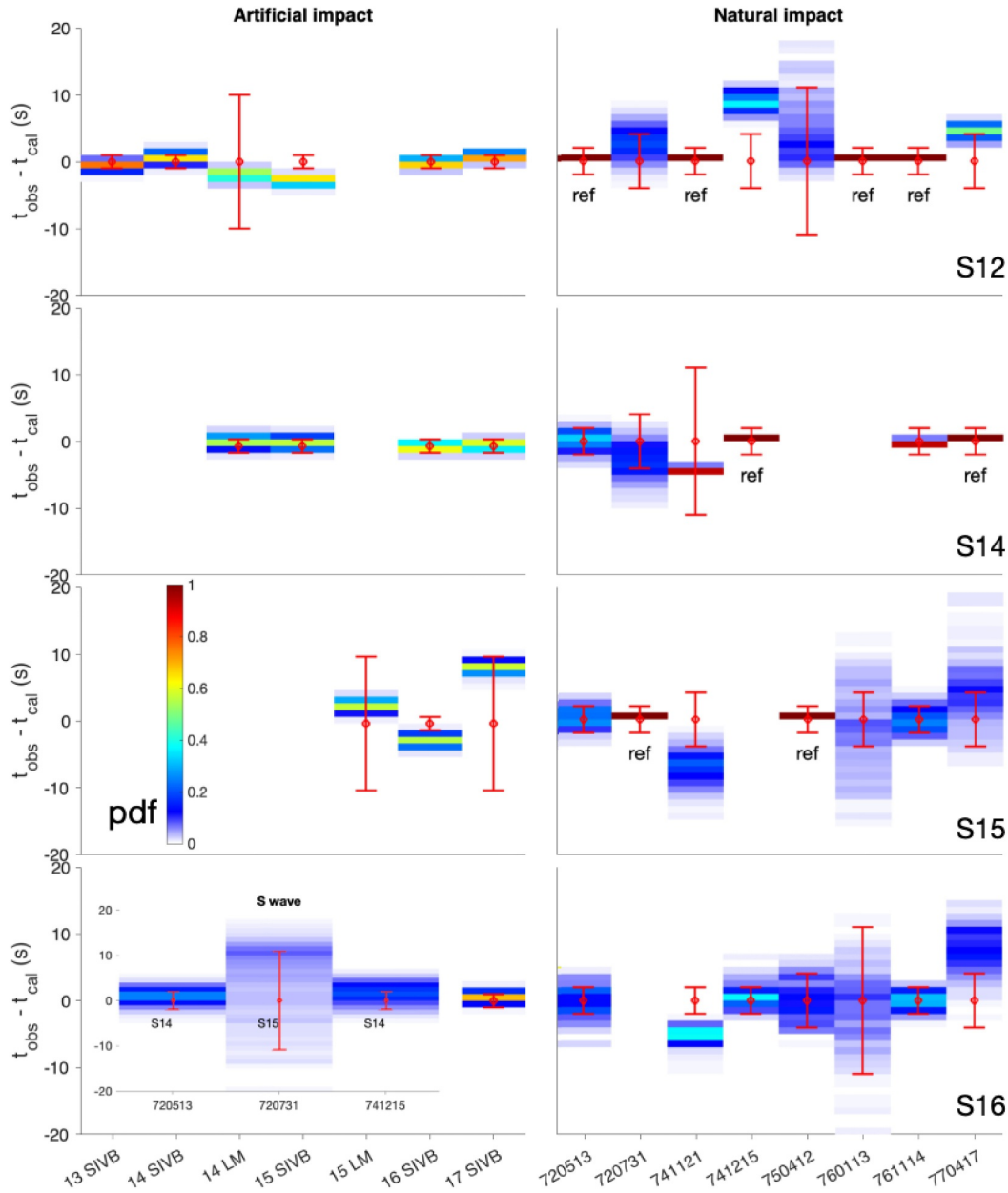

Figure 12. Data fit of the wave arrival times, considering 7 artificial impacts and 8 natural impacts, with total of 42 P-arrival times and 3 S-arrival times (displayed separately in the lower-left corner). For the artificial impacts, we compute the absolute travel time difference between observations and calculations, red lines show the arrival time reading errors. For the natural impacts, we compute the relative travel time difference between observations and calculations, red lines show the arrival time reading error of corresponding event plus the arrival time reading error of the reference event which marked 'ref' in the figure.

density, a trade-off exists between the average upper mantle density and crustal porosity. Here, we assume an upper mantle density of approximately 3,300 kg/m^3 to simultaneously satisfy the seismic and minimum crustal thickness constraints (<1 km, Wieczorek et al., 2013; Garcia et al., 2019). The 10% average lunar crustal porosity is also within the range of results from previous studies (Huang & Wieczorek, 2012; Wieczorek et al., 2013) and is consistent with porosity estimates of impact-fractured meteorites and terrestrial impact craters (Consolmagno et al., 2008; Warren, 2001).

21699100, 2026, 11, Downloaded from https://agupubs.onlinelibrary.wiley.com/doi/10.1029/2026JE009866 by Okayama University, Wiley Online Library on [11/11/2026]. See the Terms and Conditions (https://onlinelibrary.wiley.com/terms-and-conditions) on Wiley Online Library for rules of use; OA articles are governed by the applicable Creative Commons License

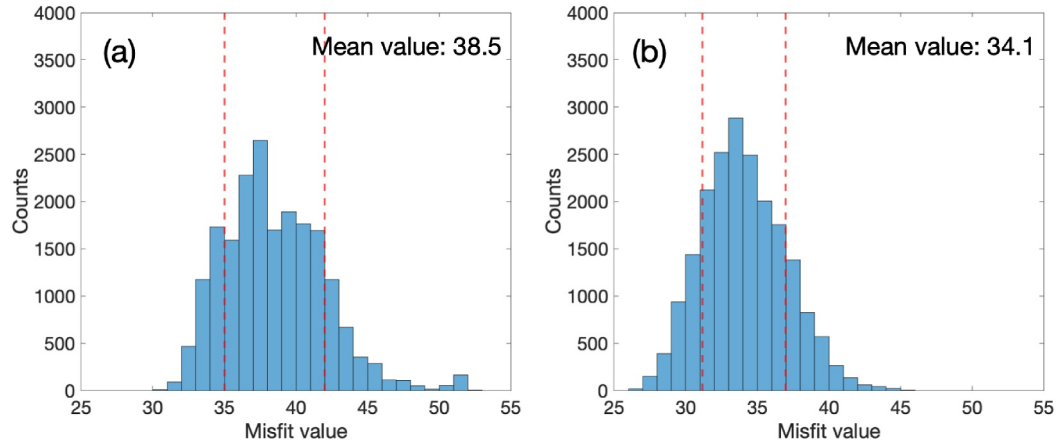

Figure 13. Histograms of misfit values for (a) 1D and (b) 3D mantle velocity models. Each panel shows the accepted misfit values, dashed red lines are the 1-σ ranges of the misfit values.

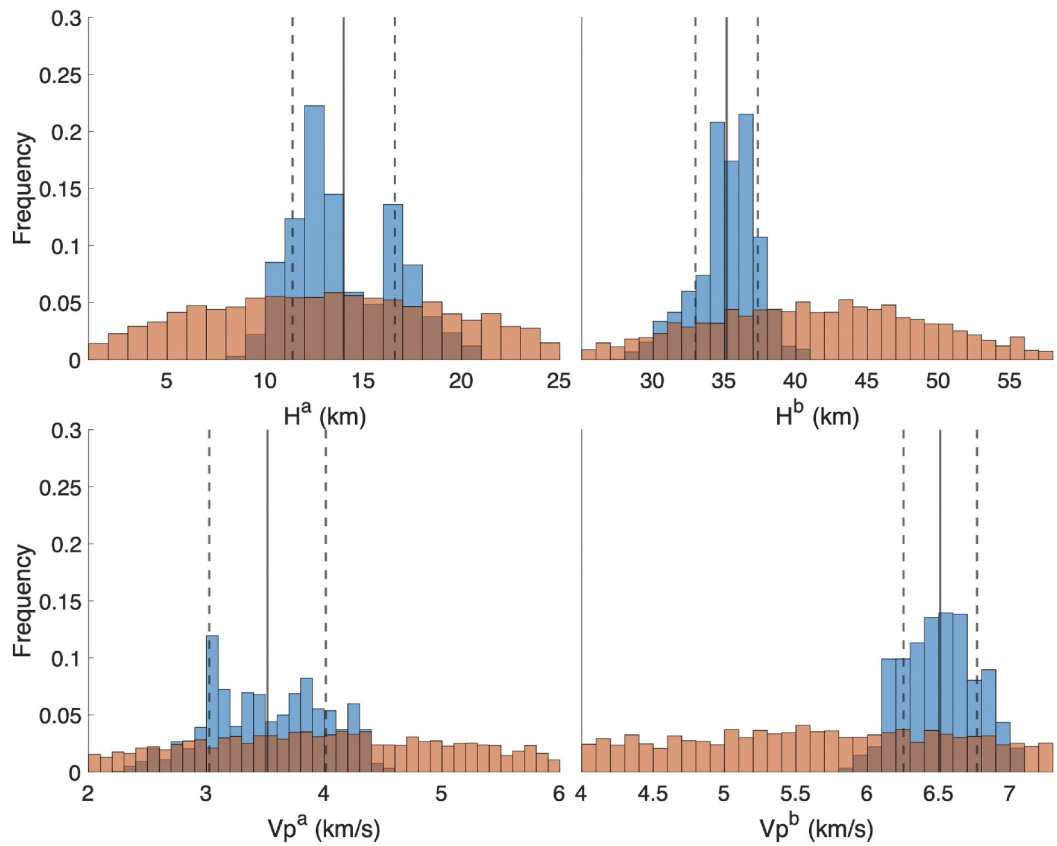

Figure 14. Marginal distributions of the inverted parameters in the crust. The orange and blue histograms correspond to the *a priori* and *a posteriori* distributions, respectively. Black lines are mean and dashed lines are 1-σ of the output values of each parameter.

21699100, 2026, 11, Downloaded from https://agupubs.onlinelibrary.wiley.com/doi/10.1029/2026JE009866 by Okayama University, Wiley Online Library on [11/11/2026]. See the Terms and Conditions (https://onlinelibrary.wiley.com/terms-and-conditions) on Wiley Online Library for rules of use; OA articles are governed by the applicable Creative Commons License

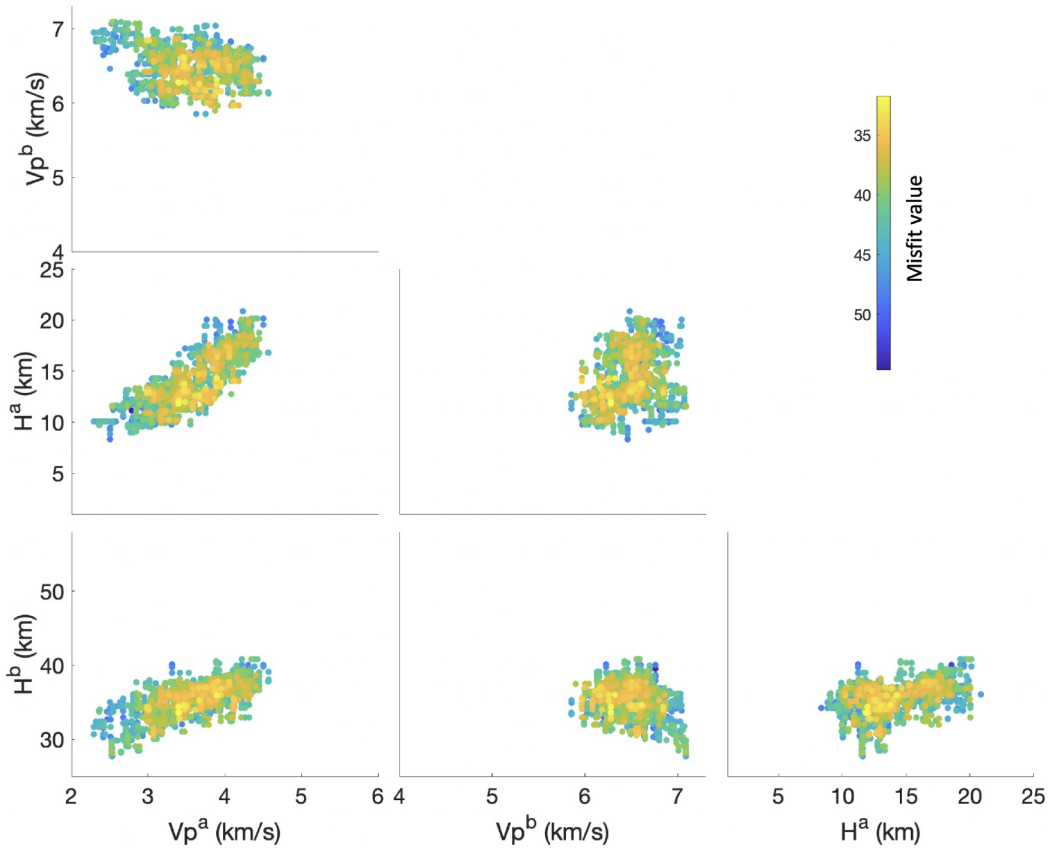

Figure 15. Correlations between the depth and the *P*-wave velocity of two crustal layers, for all the models accepted during the inversion. Yellow and blue colors indicate small and large misfit values, respectively. See also Figure S20 in Supporting Information S1 for the sampled frequencies of each pair of parameters.

Additionally, the average crustal heat source density (Q_{cr}) and the thermal conductivity (k_{cr}) are 0.42 W/mK and 480×10^{-9} W/m^3, respectively (Table S2 in Supporting Information S1). The observed surface heat flow is 21 mW/m^2 at the Apollo 15 landing site and 14 mW/m^2 at the Apollo 17 landing site based on data through the end of 1974 (Langseth et al., 1976). Adjusting the Apollo 17 heat flow for the boundary effect, Warren and Rasmussen (1987) estimated that 12 ± 1.2 mW/m^2 may be a more representative heat flow average for the global Moon. Based on the preference parameters given above, the average surface heat flow value of our 3D thermal model is 10.7 ± 0.8 mW/m^2, which is consistent with the result reported by Warren and Rasmussen (1987). NASA's Commercial Lunar Payload Services missions, Blue Ghost Mission 1 (already landed), and the Lunar Interior Temperature and Materials Suite (LITMS) will both conduct heat flow measurements on the lunar surface (Ngo et al., 2019), with the upcoming data expected to further validate our results.

Bulk Th and Al abundances are considered as a key to deciphering the bulk composition and origin of the Moon. Since a significant portion of the lunar aluminum budget resides in the crust, its global bulk concentration will necessarily be dependent upon both the average crustal thickness and the average Al_2O_3 concentration of the crust. Here, we consider the effect of variations in lunar crustal thickness on the lunar aluminum budget. If the bulk concentration of Al_2O_3 is taken as 32 wt% in the crust and 2 wt% in the mantle (Jolliff et al., 2006; Wieczorek et al., 2013), a 30 km variation in crustal thickness would lead to a 40% change in the global bulk aluminum abundance (3.51–4.99 wt%). This could cause its content to be either lower or higher than that of Earth (about 4 wt%). Based on our findings, the calculated bulk aluminum abundance is 3.76 ± 0.2 wt%. In addition, since a large portion of the lunar incompatible elements is sequestered in the crust, bulk compositional models for these

21699100, 2026, 11, Downloaded from https://agupubs.onlinelibrary.wiley.com/doi/10.1029/2026JE009866 by Okayama University, Wiley Online Library on [11/11/2026]. See the Terms and Conditions (https://onlinelibrary.wiley.com/terms-and-conditions) on Wiley Online Library for rules of use; OA articles are governed by the applicable Creative Commons License

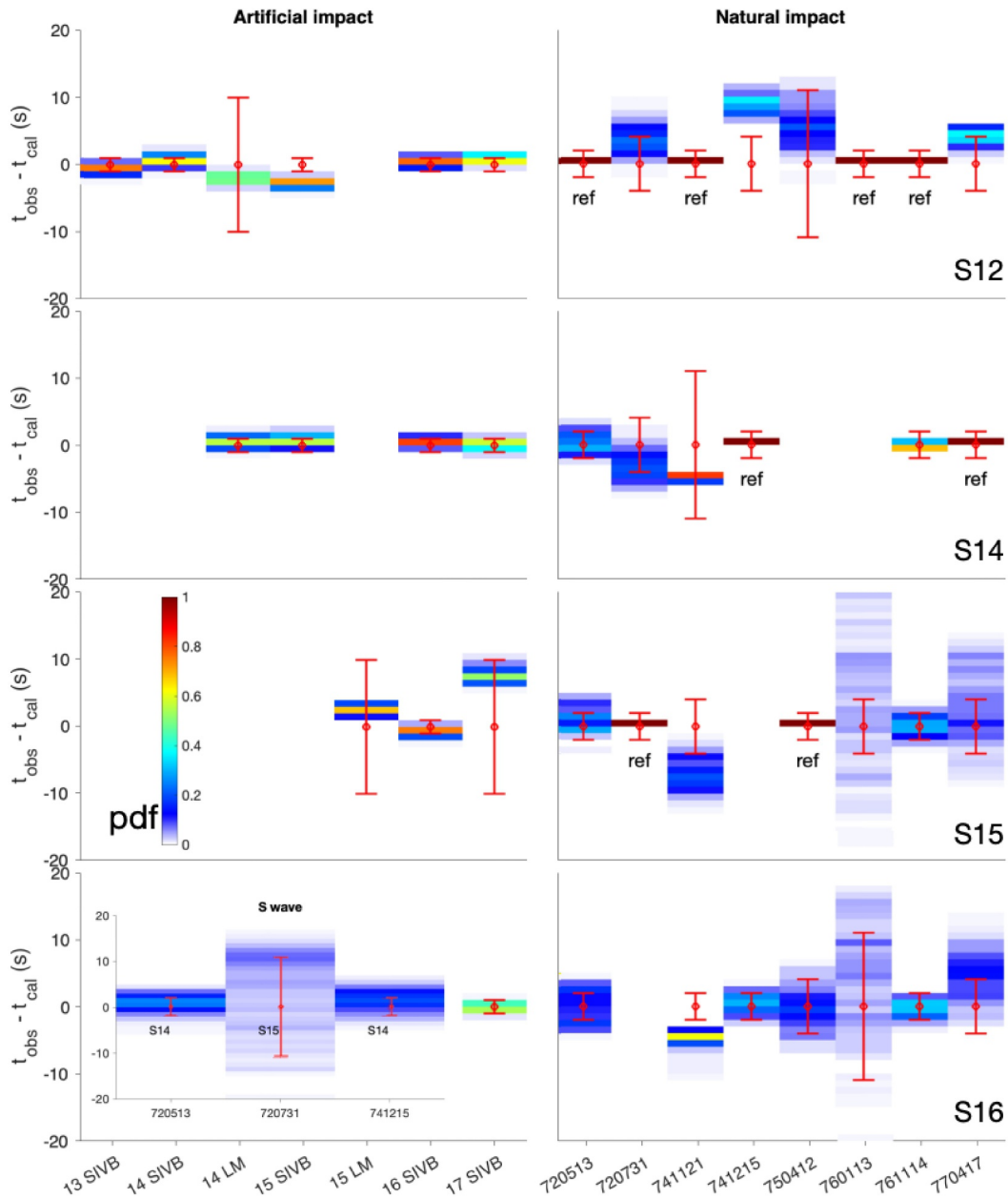

Figure 16. Data fit of the wave arrival times, considering 7 artificial impacts and 8 natural impacts, with total of 42 *P*-arrival times and 3 *S*-arrival times (displayed separately in the lower-left corner). For the artificial impacts, we compute the absolute travel time difference between observations and calculations, red lines show the arrival time reading errors. For the natural impacts, we compute the relative travel time difference between observations and calculations, red lines show the arrival time reading error of corresponding event plus the arrival time reading error of the reference event which marked 'ref' in the figure.

elements are also dependent upon the average crustal thickness. Assuming average Th abundances of 1 ppm for the entire crust and 40 ppb for the mantle (Jolliff et al., 2006), then a change in crustal thickness of 30 km would correspond to a change in the bulk Th abundance of about 47 ppb (88.6–135.8 ppb). By comparison, this study constrains the global bulk Th abundance to 96.54 ± 6 ppb. These results demonstrate that reducing the uncertainty in lunar crustal thickness can improve estimates of the bulk elemental abundances. However, it should be noted that the uncertainties in the assumed Al and Th concentrations have not been taken into account in this analysis.

21699100, 2026, 11, Downloaded from https://agupubs.onlinelibrary.wiley.com/doi/10.1029/2026JE009866 by Okayama University, Wiley Online Library on [11/11/2026]. See the Terms and Conditions (https://onlinelibrary.wiley.com/terms-and-conditions) on Wiley Online Library for rules of use; OA articles are governed by the applicable Creative Commons License

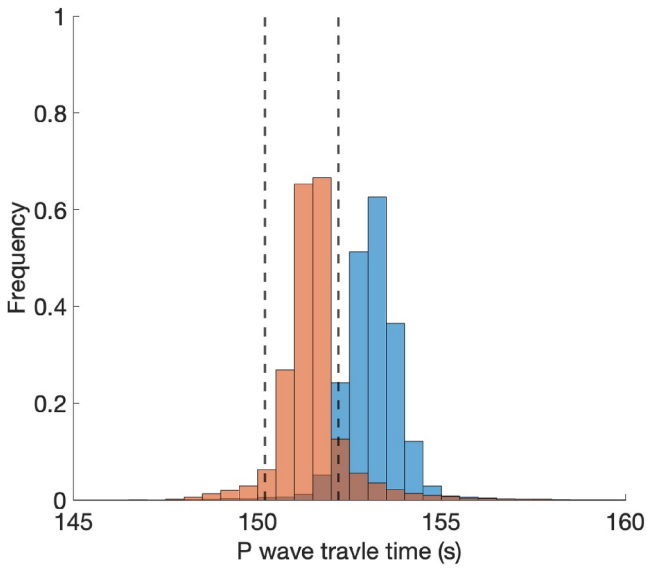

Figure 17. Histogram of inverted travel times for the artificial impact SIVB 16 recorded at Station 15, derived from 1D (blue) and 3D (orange) mantle velocity models. The black dashed lines denote the range of manually picked arrival times.

These assumed values are derived from limited lunar samples and remote sensing observations and thus carry substantial inherent uncertainties, which would further increase the overall uncertainty beyond the present error estimates.

The details of the Moon's post-magma ocean structure are also highly sensitive to assumptions about the composition, the depth of the magma ocean, and the crystallization process (Andrews-Hanna et al., 2023). The initial depth of the magma ocean is still poorly constrained, with models of its evolution typically considering values ranging from 400 km to a completely molten state. One potential constraint on the depth of the magma ocean is the predicted crustal thickness in comparison to the inferred mean crustal thickness. Uncertainties in the structure of the lunar crust lead to broader uncertainties in the thermochemical evolution of the Moon's interior (Elkins-Tanton et al., 2011; Rapp & Draper, 2018; Snyder et al., 1992). New constraints on mean crustal thickness will also reduce the uncertainty of this prediction.

Recently, lunar exploration is facing a new era with a series of landing missions planned not only by national space agencies but also by private companies. Multiple lunar landings are expected in the near future, and seismic observation is regarded as a high priority scientific payload for these missions. Among planned missions, both NASA's Farside Seismic Suite (FSS) (Panning et al., 2022), the Chinese Chang'E-7 (CE-7) (Wang et al., 2024) mission, the Lunar Environment Monitoring Station (Schmerr et al., 2024) and the South Pole Seismic Station on Artemis missions (https://science.nasa.gov/missions/artemis/artemis-4/nasa-selects-2-instruments-for-artemis-iv-lunar-surface-science/) will carry seismometers to the Moon. These launches will target the seismic exploration of the lunar farside, with landing sites near the Schrödinger Basin for FSS and South Pole for the others. Our results predict a crustal thickness of 22–28 km at the FSS landing site in Schrödinger Basin and 30–36 km at the potential CE-7 and Artemis landing sites near the lunar South Pole. This provides valuable prior constraints for investigating the structure of these regions.

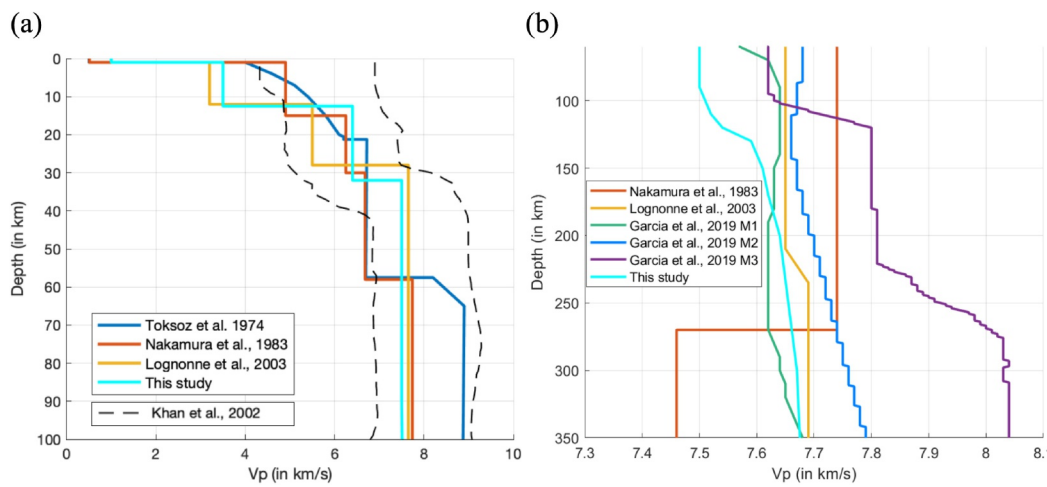

Figure 18. Comparison of the 1D lunar velocity models. (a) Lunar crust and uppermost mantle velocity models. The 1D model from this study represents the velocity structure beneath Apollo Station 12. (b) Lunar upper mantle velocity models. The cyan curve represents the average velocity profile of the nearside in our best-fitting 3D model.

21699100, 2026, 11, Downloaded from https://agupubs.onlinelibrary.wiley.com/doi/10.1029/2026JE009866 by Okayama University, Wiley Online Library on [11/11/2026]. See the Terms and Conditions (https://onlinelibrary.wiley.com/terms-and-conditions) on Wiley Online Library for rules of use; OA articles are governed by the applicable Creative Commons License

Conflict of Interest

The authors declare no conflicts of interest relevant to this study.

Availability Statement

Three-dimensional seismic velocity data of the lunar mantle, along with its one-dimensional averaged profile, are available from the Zenodo repository (Zhang et al., 2025).

Acknowledgments
The authors thank editor Jean-Pierre Williams and two anonymous reviewers for providing very helpful comments that improved the manuscript. XZ was supported by the National Key Research and Development Program of China (2022YFF0503100) and the CSC (No. 202104910134). French co-authors acknowledge the support of the French Space Agency CNES and Agence Nationale de la Recherche, ANR (ANR-19-CE31-0008-08). XZ, TK, HS, PL acknowledge the support of IdEx Université Paris Cité ANR-18-IDEX-0001. Open access publication funding provided by Universite Paris Cite.

References

Andrews-Hanna, J. C., Bottke, W. F., Broquet, A., Evans, A. J., Gowman, G., Johnson, B. C., et al. (2025). Southward impact excavated magma ocean at the lunar south pole–Aitken basin. *Nature*, *646*(8084), 297–302. https://doi.org/10.1038/s41586-025-09582-y

Andrews-Hanna, J. C., Weber, R. C., Garrick-Bethell, I., Evans, A. J., Kiefer, W. S., Grimm, R. E., et al. (2023). The structure and evolution of the lunar interior. *Reviews in Mineralogy and Geochemistry*, *89*(1), 243–292. https://doi.org/10.2138/rmg.2023.89.06

Besserer, J., Nimmo, F., Wieczorek, M. A., Weber, R. C., Kiefer, W. S., McGovern, P. J., et al. (2014). Grail gravity constraints on the vertical and lateral density structure of the lunar crust. *Geophysical Research Letters*, *41*(16), 5771–5777. https://doi.org/10.1002/2014gl060240

Blanchette-Guertin, J.-F., Johnson, C. L., & Lawrence, J. F. (2012). Investigation of scattering in lunar seismic coda. *Journal of Geophysical Research*, *117*(E6), E06003. https://doi.org/10.1029/2011je004042

Che, X., Long, T., Nemchin, A., Xie, S., Qiao, L., Li, Z., & Liu, D. (2025). Isotopic and compositional constraints on the source of basalt collected from the lunar far side. *Science*, eadt3332.

Chenet, H., Lognonné, P., Wieczorek, M., & Mizutani, H. (2006). Lateral variations of lunar crustal thickness from the apollo seismic data set. *Earth and Planetary Science Letters*, *243*(1–2), 1–14. https://doi.org/10.1016/j.epsl.2005.12.017

Connolly, J. A. (2005). Computation of phase equilibria by linear programming: A tool for geodynamic modeling and its application to subduction zone decarbonation. *Earth and Planetary Science Letters*, *236*(1–2), 524–541. https://doi.org/10.1016/j.epsl.2005.04.033

Consolmagno, G., Britt, D., & Macke, R. (2008). The significance of meteorite density and porosity. *Geochemistry*, *68*(1), 1–29. https://doi.org/10.1016/j.chemer.2008.01.003

Crotwell, H. P., Owens, T. J., & Ritsema, J. (1999). The taup toolkit: Flexible seismic travel-time and ray-path utilities. *Seismological Research Letters*, *70*(2), 154–160. https://doi.org/10.1785/gssrl.70.2.154

Drilleau, M., Samuel, H., Rivoldini, A., Panning, M., & Lognonné, P. (2021). Bayesian inversion of the Martian structure using geodynamic constraints. *Geophysical Journal International*, *226*(3), 1615–1644. https://doi.org/10.1093/gji/ggab105

Elkins-Tanton, L. T., Burgess, S., & Yin, Q.-Z. (2011). The lunar magma ocean: Reconciling the solidification process with lunar petrology and geochronology. *Earth and Planetary Science Letters*, *304*(3–4), 326–336. https://doi.org/10.1016/j.epsl.2011.02.004

Gagnepain-Beyneix, J., Lognonné, P., Chenet, H., Lombardi, D., & Spohn, T. (2006). A seismic model of the lunar mantle and constraints on temperature and mineralogy. *Physics of the Earth and Planetary Interiors*, *159*(3–4), 140–166. https://doi.org/10.1016/j.pepi.2006.05.009

Garcia, R. F., Gagnepain-Beyneix, J., Chevrot, S., & Lognonné, P. (2011). Very preliminary reference moon model. *Physics of the Earth and Planetary Interiors*, *188*(1–2), 96–113. https://doi.org/10.1016/j.pepi.2011.06.015

Garcia, R. F., Khan, A., Drilleau, M., Margerin, L., Kawamura, T., Sun, D., et al. (2019). Lunar seismology: An update on interior structure models. *Space Science Reviews*, *215*(8), 50. https://doi.org/10.1007/s11214-019-0613-y

Gillet, K., Margerin, L., Calvet, M., & Monnereau, M. (2017). Scattering attenuation profile of the moon: Implications for shallow moonquakes and the structure of the megaregolith. *Physics of the Earth and Planetary Interiors*, *262*, 28–40. https://doi.org/10.1016/j.pepi.2016.11.001

Goins, N. R., Dainty, A., & Toksöz, M. (1981). Lunar seismology: The internal structure of the moon. *Journal of Geophysical Research*, *86*(B6), 5061–5074. https://doi.org/10.1029/jb086ib06p05061

Gong, S., Wieczorek, M. A., Nimmo, F., Kiefer, W. S., Head, J. W., Huang, C., et al. (2016). Thicknesses of mare basalts on the moon from gravity and topography. *Journal of Geophysical Research: Planets*, *121*(5), 854–870. https://doi.org/10.1002/2016je005008

Huang, Q., & Wieczorek, M. A. (2012). Density and porosity of the lunar crust from gravity and topography. *Journal of Geophysical Research*, *117*(E5), E05003. https://doi.org/10.1029/2012je004062

Jolliff, B. L., Wieczorek, M. A., Shearer, C. K., & Neal, C. R. (2006). *New views of the moon* (Vol. 60). Mineralogical Society of America.

Kawamura, T., Lognonné, P., Nishikawa, Y., & Tanaka, S. (2017). Evaluation of deep moonquake source parameters: Implication for fault characteristics and thermal state. *Journal of Geophysical Research: Planets*, *122*(7), 1487–1504. https://doi.org/10.1002/2016JE005147

Khan, A., Maclennan, J., Taylor, S. R., & Connolly, J. A. (2006). Are the Earth and the moon compositionally alike? Inferences on lunar composition and implications for lunar origin and evolution from geophysical modeling. *Journal of Geophysical Research*, *111*(E5), E05005. https://doi.org/10.1029/2005je002608

Khan, A., & Mosegaard, K. (2002). An inquiry into the lunar interior: A nonlinear inversion of the apollo lunar seismic data. *Journal of Geophysical Research*, *107*(E6), 3-1–3-23. https://doi.org/10.1029/2001je001658

Khan, A., Mosegaard, K., & Rasmussen, K. L. (2000). A new seismic velocity model for the moon from a monte carlo inversion of the apollo lunar seismic data. *Geophysical Research Letters*, *27*(11), 1591–1594. https://doi.org/10.1029/1999gl008452

Khan, A., Pommier, A., Neumann, G., & Mosegaard, K. (2013). The lunar MOHO and the internal structure of the moon: A geophysical perspective. *Tectonophysics*, *609*, 331–352. https://doi.org/10.1016/j.tecto.2013.02.024

Kim, D., Lekić, V., Wieczorek, M., Schmerr, N., Collins, G., & Panning, M. (2025). A new lunar crustal thickness model constrained by converted seismic waves detected beneath the apollo seismic network. *Geophysical Research Letters*, *52*(13), e2024GL114506. https://doi.org/10.1029/2024gl114506

Laneuville, M., Taylor, J., & Wieczorek, M. (2018). Distribution of radioactive heat sources and thermal history of the moon. *Journal of Geophysical Research: Planets*, *123*(12), 3144–3166. https://doi.org/10.1029/2018je005742

Laneuville, M., Wieczorek, M., Breuer, D., & Tosi, N. (2013). Asymmetric thermal evolution of the moon. *Journal of Geophysical Research: Planets*, *118*(7), 1435–1452. https://doi.org/10.1002/jgre.20103

Langseth, M. G., Keihm, S. J., & Peters, K. (1976). Revised lunar heat-flow values. In *Lunar science conference, 7th, Houston, tex* (Vol. 7, pp. 3143–3171). Pergamon Press. march 15-19, 1976.

Lognonné, P., Gagnepain-Beyneix, J., & Chenet, H. (2003). A new seismic model of the moon: Implications for structure, thermal evolution and formation of the moon. *Earth and Planetary Science Letters*, *211*(1–2), 27–44. https://doi.org/10.1016/s0012-821x(03)00172-9

21699100, 2026, 11, Downloaded from https://agupubs.onlinelibrary.wiley.com/doi/10.1029/2026JE009866 by Okayama University, Wiley Online Library on [11/11/2026]. See the Terms and Conditions (https://onlinelibrary.wiley.com/terms-and-conditions) on Wiley Online Library for rules of use; OA articles are governed by the applicable Creative Commons License

Magali, J. K., Bodin, T., Hedjazian, N., Samuel, H., & Atkins, S. (2021). Geodynamic tomography: Constraining upper-mantle deformation patterns from Bayesian inversion of surface waves. *Geophysical Journal International*, *224*(3), 2077–2099. https://doi.org/10.1093/gji/ggaa577

Melosh, H., Kendall, J., Horgan, B., Johnson, B., Bowling, T., Lucey, P., & Taylor, G. (2017). South pole–Aitken basin ejecta reveal the moon's upper mantle. *Geology*, *45*(12), 1063–1066. https://doi.org/10.1130/g39375.1

Nakamura, Y. (1983). Seismic velocity structure of the lunar mantle. *Journal of Geophysical Research*, *88*(B1), 677–686. https://doi.org/10.1029/jb088ib01p00677

Ngo, P., Nagihara, S., Sanigepalli, V., Sanasarian, L., & Zacny, K. (2019). Heat flow probe for short-duration lander missions under nasa's commercial lunar payload service program. *Agu fall meeting abstracts*, *2019*, P33C–05.

Nolet, G. (2008). *A breviary of seismic tomography: Imaging the interior of the Earth and sun*. Cambridge University Press.

O'Neill, H. S. C. (2005). Mantle composition. *The Mantle and Core: Treatise on Geochemistry*, *2*(2), 1.

Onodera, K., Kawamura, T., Tanaka, S., Ishihara, Y., & Maeda, T. (2021). Numerical simulation of lunar seismic wave propagation: Investigation of subsurface scattering properties near apollo 12 landing site. *Journal of Geophysical Research: Planets*, *126*(3), e2020JE006406. https://doi.org/10.1029/2020je006406

Onodera, K., Kawamura, T., Tanaka, S., Ishihara, Y., & Maeda, T. (2022). Quantitative evaluation of the lunar seismic scattering and comparison between the Earth, Mars, and the moon. *Journal of Geophysical Research: Planets*, *127*(12), e2022JE007558. https://doi.org/10.1029/2022je007558

Panning, M., Kedar, S., Bowles, N., Bugby, D., Calcutt, S., Cutler, J., et al. (2022). Farside seismic suite (fss): Surviving the lunar night and delivering the first seismic data from the farside of the moon. *53rd lunar and planetary science conference*, *2678*, 1576.

Potter, R. W., Collins, G. S., Kiefer, W. S., McGovern, P. J., & Kring, D. A. (2012). Constraining the size of the south pole-Aitken basin impact. *Icarus*, *220*(2), 730–743. https://doi.org/10.1016/j.icarus.2012.05.032

Rapp, J., & Draper, D. (2018). Fractional crystallization of the lunar magma ocean: Updating the dominant paradigm. *Meteoritics and Planetary Science*, *53*(7), 1432–1455. https://doi.org/10.1111/maps.13086

Schmerr, N., Benna, M., McCall, N., Bailey, S., DellaGiustina, D., Bray, V., et al. (2024). The lunar environmental monitoring station: An artemis 3 deployed instrument. *LPI Contribution*, *3060*, 6010.

Schumacher, S., & Breuer, D. (2006). Influence of a variable thermal conductivity on the thermochemical evolution of Mars. *Journal of Geophysical Research*, *111*(E2), E02006. https://doi.org/10.1029/2005je002429

Shi, J., Wang, T., Chen, H., Yang, M., Chen, L., Hui, H., et al. (2023). Differences in scattering properties of the shallow crusts of Earth, Mars, and the moon revealed by p-wave receiver functions. *Journal of Geophysical Research: Planets*, *128*(8), e2022JE007676. https://doi.org/10.1029/2022je007676

Simmons, G., Todd, T., & Wang, H. (1973). The 25-km discontinuity: Implications for lunar history. *Science*, *182*(4108), 158–161. https://doi.org/10.1126/science.182.4108.158

Smith, D. E., Zuber, M. T., Jackson, G. B., Cavanaugh, J. F., Neumann, G. A., Riris, H., et al. (2010). The lunar orbiter laser altimeter investigation on the lunar reconnaissance orbiter mission. *Space Science Reviews*, *150*(1–4), 209–241. https://doi.org/10.1007/s11214-009-9512-y

Snyder, G. A., Taylor, L. A., & Neal, C. R. (1992). A chemical model for generating the sources of mare basalts: Combined equilibrium and fractional crystallization of the lunar magmasphere. *Geochimica et Cosmochimica Acta*, *56*(10), 3809–3823. https://doi.org/10.1016/0016-7037(92)90172-f

Sobolev, S. V., & Babeyko, A. Y. (1994). Modeling of mineralogical composition, density and elastic wave velocities in anhydrous magmatic rocks. *Surveys in Geophysics*, *15*(5), 515–544. https://doi.org/10.1007/bf00690173

Steinhart, J. (1967). Mohorovicic discontinuity. *International dictionary of geophysics*, *2*, 991–994.

Toksőz, M., Press, F., Anderson, K., Dainty, A., Latham, G., Ewing, M., et al. (1972). Velocity structure and properties of the lunar crust. *The moon*, *4*(3–4), 490–504. https://doi.org/10.1007/bf00562013

Toksöz, M. N., Dainty, A. M., Solomon, S. C., & Anderson, K. R. (1974). Structure of the moon. *Reviews of Geophysics*, *12*(4), 539–567.

Torrent Duch, A., Garcia, R. F., & Drilleau, M. (2025). The moon's crust and upper mantle discontinuities revealed by seismic interferometry methods applied to apollo seismic data. *Journal of Geophysical Research: Planets*, *130*(12), e2025JE009090. https://doi.org/10.1029/2025je009090

Turcotte, D. L., & Schubert, G. (2002). In *Geodynamics* (2nd ed.).

Vinnik, L., Chenet, H., Gagnepain-Beyneix, J., & Lognonne, P. (2001). First seismic receiver functions on the moon. *Geophysical Research Letters*, *28*(15), 3031–3034. https://doi.org/10.1029/2001gl012859

Wang, C., Jia, Y., Xue, C., Lin, Y., Liu, J., Fu, X., et al. (2024). Scientific objectives and payload configuration of the chang'e-7 mission. *National Science Review*, *11*(2), nwad329. https://doi.org/10.1093/nsr/nwad329

Warren, P. H. (2001). Porosities of lunar meteorites: Strength, porosity, and petrologic screening during the meteorite delivery process. *Journal of Geophysical Research*, *106*(E5), 10101–10111. https://doi.org/10.1029/2000je001283

Warren, P. H. (2005). "new" lunar meteorites: Implications for composition of the global lunar surface, lunar crust, and the bulk moon. *Meteoritics and Planetary Science*, *40*(3), 477–506. https://doi.org/10.1111/j.1945-5100.2005.tb00395.x

Warren, P. H., & Rasmussen, K. L. (1987). Megaregolith insulation, internal temperatures, and bulk uranium content of the moon. *Journal of Geophysical Research*, *92*(B5), 3453–3465. https://doi.org/10.1029/jb092ib05p03453

Wieczorek, M. A., Neumann, G. A., Nimmo, F., Kiefer, W. S., Taylor, G. J., Melosh, H. J., et al. (2013). The crust of the moon as seen by grail. *Science*, *339*(6120), 671–675. https://doi.org/10.1126/science.1231530

Wieczorek, M. A., & Phillips, R. J. (1997). The structure and compensation of the lunar highland crust. *Journal of Geophysical Research*, *102*(E5), 10933–10943. https://doi.org/10.1029/97je00666

Zhang, X., Kawamura, T., Drilleau, M., Lognonné, P., Samuel, H., Xu, Z., et al. (2026). Lateral variations in lunar crustal thickness inferred from apollo seismic and grail gravity data. *Journal of Geophysical Research: Planets*, *131*(5), e2025JE009453. https://doi.org/10.1029/2025je009453

Zhang, X., Lognonné, P., samuel, h., Kawamura, T., Drilleau, M., Wieczorek, M., et al. (2025). Three-dimensional seismic p-wave velocity model of the lunar mantle (version v1) [dataset]. *Zenodo*. https://doi.org/10.5281/zenodo.15727652

Ziethe, R., Seiferlin, K., & Hiesinger, H. (2009). Duration and extent of lunar volcanism: Comparison of 3d convection models to mare basalt ages. *Planetary and Space Science*, *57*(7), 784–796. https://doi.org/10.1016/j.pss.2009.02.002

21699100, 2026, 11, Downloaded from https://agupubs.onlinelibrary.wiley.com/doi/10.1029/2026JE009866 by Okayama University, Wiley Online Library on [11/11/2026]. See the Terms and Conditions (https://onlinelibrary.wiley.com/terms-and-conditions) on Wiley Online Library for rules of use; OA articles are governed by the applicable Creative Commons License

References From the Supporting Information

Brandt, A. (1982). Guide to multigrid development. *Lecture Notes in Mathematics*, *960*, 220–312. https://doi.org/10.1007/bfb0069930

Cooper, M. R., Kovach, R. L., & Watkins, J. S. (1974). Lunar near-surface structure. *Reviews of Geophysics*, *12*(3), 291–308.

Karato, S.-I., & Wu, P. (1993). Rheology of the upper mantle: A synthesis. *Science*, *260*(5109), 771–778. https://doi.org/10.1126/science.260.5109.771

Luo, K., Zhuang, Z., Fan, J., & Haugen, N. E. L. (2016). A ghost-cell immersed boundary method for simulations of heat transfer in compressible flows under different boundary conditions. *International Journal of Heat and Mass Transfer*, *92*, 708–717. https://doi.org/10.1016/j.ijheatmasstransfer.2015.09.024

Nimmo, F., Faul, U. H., & Garnero, E. J. (2012). Dissipation at tidal and seismic frequencies in a melt-free moon. *Journal of Geophysical ResearchEducational Planning*, *117*(9), E09005. https://doi.org/10.1029/2012JE004160

Simmons, G., Siegfried, R., & Richter, D. (1975). Characteristics of microcracks in lunar samples. In *Lunar science conference* (Vol. 6, pp. 3227–3254).

Sondergeld, C., Granryd, L., & Spetzler, H. (1979). Compressional velocity measurements for a highly fractured lunar anorthosite. In *Lunar and planetary science conference* (Vol. 10, pp. 2147–2154).

Weber, R. C., Lin, P.-Y., Garnero, E. J., Williams, Q., & Phillips, P. (2011). Seismic detection of the lunar core. *Science*, *331*(6015), 309–312. https://doi.org/10.1126/science.1199375

Wieczorek, M. A. (2015). Gravity and topography of the terrestrial planets. *Treatise on geophysics*, *10*, 165–206.

Wieczorek, M. A., Jolliff, B. L., Khan, A., Pritchard, M. E., Weiss, B. P., & Williams, J. G. (2006). The constitution and structure of the lunar interior. *Reviews in Mineralogy and Geochemistry*, *60*(1), 221–364.

Wieczorek, M. A., & Phillips, R. J. (1998). Potential anomalies on a sphere: Applications to the thickness of the lunar crust. *Journal of Geophysical Research*, *103*(E1), 1715–1724. https://doi.org/10.1029/97je03136

Yanagisawa, T., Kameyama, M., & Ogawa, M. (2016). Numerical studies on convective stability and flow pattern in three-dimensional spherical mantle of terrestrial planets. *Geophysical Journal International*, *206*(3), 1526–1538. https://doi.org/10.1093/gji/ggw226

21699100, 2026, 11, Downloaded from https://agupubs.onlinelibrary.wiley.com/doi/10.1029/2026JE009866 by Okayama University, Wiley Online Library on [11/11/2026]. See the Terms and Conditions (https://onlinelibrary.wiley.com/terms-and-conditions) on Wiley Online Library for rules of use; OA articles are governed by the applicable Creative Commons License